Bioactive Materials 28 (2023) 95–111

Contents lists available at ScienceDirect

Bioactive Materials

journal homepage: www.keaipublishing.com/en/journals/bioactive-materials

Tailoring the multiscale mechanics of tunable decellularized extracellular matrix (dECM) for wound healing through immunomodulation

Pu Luo [a,1], Ruoxuan Huang [a,1], You Wu [a,1], Xingchen Liu [a], Zhengjie Shan [a], Li Gong [c], Shudan Deng [a], Haiwen Liu [a], Jinghan Fang [e,b], Shiyu Wu [a], Xiayi Wu [a], Quan Liu [a], Zetao Chen [a], Kelvin W.K. Yeung [e,b], Wei Qiao [d,***], Shoucheng Chen [a,**], Zhuofan Chen [a,*]

[a] Hospital of Stomatology, Sun Yat-sen University, Guangdong Provincial Key Laboratory of Stomatology, Guangdong Research Center for Dental and Cranial Rehabilitation and Material Engineering, Guangzhou, 510055, China
[b] Department of Orthopaedics and Traumatology, Li Ka Shing Faculty of Medicine, The University of Hong Kong, Hong Kong Special Administrative Region
[c] Instrumental Analysis Research Center, Sun Yat-sen University, Guangzhou, 510275, China
[d] Applied Oral Sciences and Community Dental Care, Faculty of Dentistry, The University of Hong Kong, Hong Kong Special Administrative Region
[e] Shenzhen Key Laboratory for Innovative Technology in Orthopaedic Trauma, The University of Hong Kong-Shenzhen Hospital, Shenzhen, 518058, China

ARTICLE INFO

Keywords:
Wound healing
Decellularized extracellular matrix
Freeze-thaw treatment
Multiscale mechanics
Macrophage polarization
Immunomodulation
Mechanotransduction

ABSTRACT

With the discovery of the pivotal role of macrophages in tissue regeneration through shaping the tissue immune microenvironment, various immunomodulatory strategies have been proposed to modify traditional biomaterials. Decellularized extracellular matrix (dECM) has been extensively used in the clinical treatment of tissue injury due to its favorable biocompatibility and similarity to the native tissue environment. However, most reported decellularization protocols may cause damage to the native structure of dECM, which undermines its inherent advantages and potential clinical applications. Here, we introduce a mechanically tunable dECM prepared by optimizing the freeze-thaw cycles. We demonstrated that the alteration in micromechanical properties of dECM resulting from the cyclic freeze-thaw process contributes to distinct macrophage-mediated host immune responses to the materials, which are recently recognized to play a pivotal role in determining the outcome of tissue regeneration. Our sequencing data further revealed that the immunomodulatory effect of dECM was induced via the mechnotrasduction pathways in macrophages. Next, we tested the dECM in a rat skin injury model and found an enhanced micromechanical property of dECM achieved with three freeze-thaw cycles significantly promoted the M2 polarization of macrophages, leading to superior wound healing. These findings suggest that the immunomodulatory property of dECM can be efficiently manipulated by tailoring its inherent micromechanical properties during the decellularization process. Therefore, our mechanics-immunomodulation-based strategy provides new insights into the development of advanced biomaterials for wound healing.

1. Introduction

Wound healing is a complex process mediated by cellular and molecular interactions. Impaired wound healing may lead to functional disorders and aesthetic complications, reducing the patients' quality of life and increasing the global disease burden [1]. The decellularized extracellular matrix (dECM) has a wide range of biogenic sources, favorable biocompatibility, and biodegradability. It preserves the native 3D biological structure of the tissue environment, making it a mainstream clinical tool in multiple tissue regeneration (Fig. S1, Supporting **Information**) [2–5]. Despite its widespread applications, studies have indicated that the wound healing, re-epithelialization, and appendix regeneration efficacy of dECM remains unsatisfactory, especially in diabetes mellitus patients [6,7]. Moreover, with increasing demand for

Peer review under responsibility of KeAi Communications Co., Ltd.
* Corresponding author.
** Corresponding author.
*** Corresponding author.
E-mail addresses: drqiao@hku.hk (W. Qiao), chenshch8@mail.sysu.edu.cn (S. Chen), chzhuof@mail.sysu.edu.cn (Z. Chen).
[1] The authors contributed equally.

https://doi.org/10.1016/j.bioactmat.2023.05.011
Received 12 February 2023; Received in revised form 10 May 2023; Accepted 11 May 2023

functional tissue regeneration, the aims of dECM research have evolved from achieving complete decellularization to maintaining superior bioactivity through the preservation of its inherent physicochemical cues and biological signals.

The immune microenvironment influences numerous physiological processes involved in wound healing, such as angiogenesis, re-epithelialization, and tissue remodeling. Macrophages, as the key regulators of the immune microenvironment, are extensively involved in wound healing, and play a pivotal role in phenotypic and functional changes [8,9]. M1-like macrophages exert pro-inflammatory functions by releasing pro-inflammatory cytokines to fight infection and clear dying neutrophils; however, prolonged inflammation could delay the healing process. Meanwhile, M2-like macrophages promote tissue regeneration by resolving inflammation, secreting growth factors, and recruiting epithelial cells, fibroblasts, and endotheliocytes to accelerate wound healing [10,11]. Active tuning of the polarization of macrophages holds great promise for promoting soft tissue regeneration [12,13].

Given the critical role of macrophage in determining the clinical outcome of implantable biomaterials, immunomodulatory biomaterials designed to regulate the polarization of macrophages have attracted great attention in the field of tissue engineering. Several strategies have been proposed to endow conventional dECM with the capacity to regulate macrophage phenotypes. For example, the incorporation of stimulating factors is one of the research hotspots. However, it has several limitations, including the complex preparation process, high costs, short duration of action, and potential clinical safety risks [14,15]. Composite materials offer another alternative, but they are usually associated with reduced biocompatibility and disruption of the native structure [6,16]. It remains difficult to endow dECM with good immunomodulatory while preserving its native structure.

Macrophages can sense multiple microenvironmental signals, like mechanical cues that can modulate macrophage polarization [17]. In brief, low elastic modulus (11 kPa and 88 kPa) induces macrophage polarization toward the M1 phenotype, while medium elastic modulus (0.3 MPa) promotes M2 phenotype [18]. Atcha et al. found that macrophages cultured on stiffer (20 and 280 kPa) polyacrylamide gels secreted more inflammatory cytokines and formed more multinucleated giant cells than cells cultured on soft (1 kPa) polyacrylamide gels [19]. These findings suggest that the modulation of macrophage can be achieved through tailoring the inherent mechanical properties of biomaterials. Nevertheless, our understanding of mechanoimmunology is still in its infancy [20]. For example, the *in vivo* study concerning the mechanotransduction of macrophages in response to implantable biomaterials remain scarce [19,21].

Cyclic freeze-thawing marks one of the earliest physical attempts to achieve the decellularization of ECM [22]. It is now still widely used as a cost-effective way to prepare dECM for biomedical applications [23,24]. However, recent studies reported that extensive cyclic freeze-thawing processes can lead to more severe immune responses and impair the biological performance of dECM [25]. This is controversial to traditional views suggesting the immune response caused by dECM can be alleviated through thoroughly decellularization with more cycles of freeze-thaw treatment [26]. Indeed, the microstructure of collagen at molecular and fibril-levels can be gradually modified by ice formation and interstitial fluid transport in the process of freeze-thaw treatment, leading to altered elastic modulus of the scaffolds [6,27–30]. However, the influence of these structural and mechanical changes on host tissue responses, as well as the underlying mechanisms, remain unclear. Therefore, it is essential to further explore the crosstalk between host immune system and mechanical cues at the molecular level (nanomechanical properties), cellular level (micromechanical properties), and organ level (macromechanical properties) [31].

Herein, we introduce a mechanically tunable dECM and a potent mechanics-immunomodulation-based strategy capable of accelerating wound healing. First, the mechanical properties of the dECM across multiple length scales were systemically investigated using a combination of multiple characterization methods. Moreover, the biocompatibility, biodegradation, and immunomodulatory properties of the novel dECM were investigated *in vitro* and *in vivo*. Importantly, we revealed the central role of mechanotransduction in the regulation of macrophage polarization and demonstrated the efficacy of the mechanically tunable dECM in promoting full-thickness wound healing in a rat model. Therefore, the finding of our study offers an efficient and effective approach for the development of biomaterials for wound healing.

2. Results and discussion

2.1. Preparation and characterization of the freeze-thaw treated dECM

The main difficulty in fabricating dECM with outstanding biological function is designing a powerful and efficient decellularization protocol [23]. In this study, we prepared dECM with repeated freeze-thaw circles (n = 0, 3, 7 named Control, F/T 3, and F/T 7, respectively) by using various decellularization methods. The dECM scaffolds obtained from porcine peritoneum underwent decellularization procedures, including treatment with repeated freeze-thaw cycles, alkalies and acids, organic solvents, and hypotonic and hypertonic solutions and post-decellularization procedures like lyophilization and sterilization (Fig. 1A and B). Although −20 °C and −80 °C were commonly used temperature for freeze-thaw treatment, they require much more time to thoroughly remove the cellular composition [32]. In this study, the porcine peritoneum was frozen in liquid nitrogen for 5 min and thawed at room temperature for a freeze-thaw cycle.

The goal of decellularization is to efficiently remove cells while maximally retaining ECM proteins and the native matrix structure. Histological staining dECM (Control, F/T 3, and F/T 7) confirmed effective decellularization with no visible nuclei (Fig. 1C). The quantification result of DNA content in all three groups (Control, F/T 3, and F/T 7) revealed no significant differences, and the DNA content of dECM in all three groups met the suggested criterion of below 50 ng/mg dry weight, as specified in the literature (Fig. 1G). The remaining porous structure can facilitate cell penetration, migration, nutrient transport, and removal of metabolites [33]. Considering that exposure of the secondary conformation of collagen fibrils causes severe adverse immune responses, differential scanning calorimetry (DSC), attenuated total reflectance Fourier transformed infrared (ATR-FTIR), energy dispersive spectroscopy (EDS) and X-ray diffraction (XRD) were used to further confirm the structural integrity of collagen [34]. The endothermic peaks are associated with the transformation of collagen from a triple helical to a random coil structure, with the peak value assigned to the denaturation temperature (Td) [35]. The typical range of Td for collagen's stable triple helical structure, formed by the peptide $(Pro\text{-}Hyp\text{-}Gly)_{10}$ and facilitated by interchain hydrogen bonds, ranges from 60 °C to 90 °C [35,36]. In our study, we observed a higher endothermic peak of 80.3 °C in F/T 3 group compared with 77.7 °C in the control group (Fig. 1D). This suggests the presence of more hydrogen bonds responsible for the stabilization of the triple helix of collagen. Therefore, the shift of endothermic peak in DCS test is generally accepted as an indicator for the integrity of original triple helical structure [37,38]. The broad band around 3500 cm^{-1} (amide A) associated with NH_2 bonding, the peak at 1647 cm^{-1} (amide I) associated with the stretching vibrations of the carbonyl groups, the peak at 1550 cm^{-1} (amide II) associated with the vibrational source of both NH deformation and CN stretching and peak at 1241 cm^{-1} (amide III) associated with CN stretching and NH bending vibrations in FTIR spectra were the most significant characteristics of the collagen triplex helix structure [30]. As a sensitive marker of the peptide conformation, these characteristics peaks were observed in the spectra of all three groups (Fig. 1E), suggesting the decellularization methods did not damage the secondary structure of native collagen [39]. Further, the EDS maps confirmed the existence and homogeneous distribution of C, N, O, Na, Mg, Al, P and S elements, and the EDS spectra showed

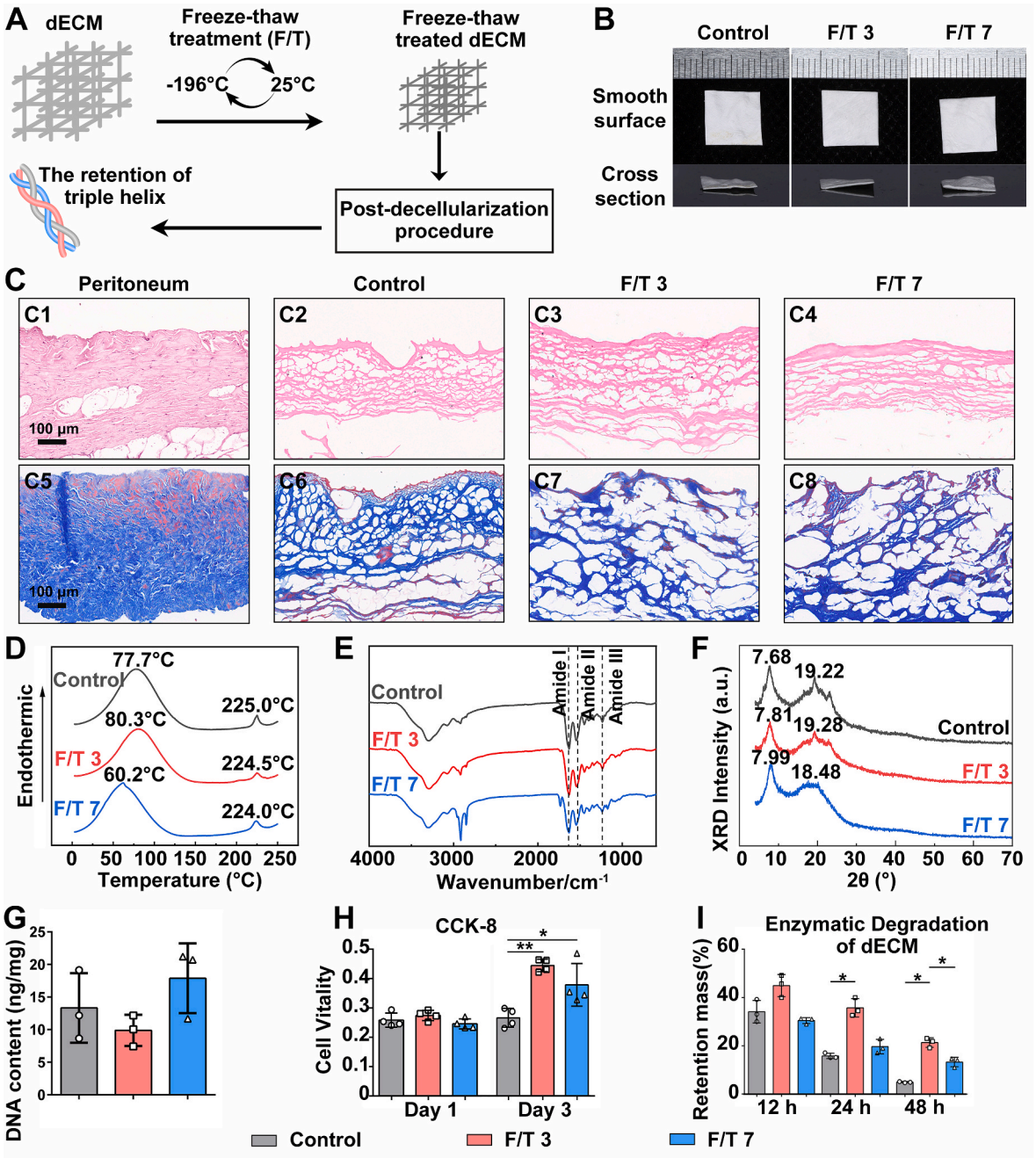

Fig. 1. Preparation and characterization of freeze-thaw treated dECM. **(A)** The schematic diagram showing the workflow for the fabrication of freeze-thaw (F/T) treated dECM. Freeze-thaw treated dECM was fabricated from porcine peritoneum with decellularization procedure and post-decellularization procedure, followed by the verification of dECM structure stability. **(B)** Representative photographs for dECM without F/T (control), F/T 3, and F/T 7 were shown. **(C)** H&E staining (C1–C4) and Masson's trichrome staining (C5–C8) of native tissue and dECM membrane to determine the efficiency of decellularization. **(D–F)** DSC curves (D), FTIR spectra (E), and XRD patterns (F) of control, F/T 3, and F/T 7 dECM, demonstrating the retention of characteristic structure in collagen. **(G)** Quantification of DNA content after decellularization. **(H)** Cell viability of macrophages cultured within the dECM for 1 and 3 days evaluated using CCK-8 assay. **(I)** *E*nzymatic degradation of dECM measured *in vitro*.

Statistical analysis was performed using ANOVA and multiple comparisons post-hoc tests (Tukey HSD). $^{*}p < 0.05$, $^{**}p < 0.01$.

similar content of elements in three groups (Fig. S4, Supporting **Information**). As shown in Fig. 1F, dECM from all three groups showed a peak at 7°–8° corresponding to the triple helix of collagen and a broad peak around 20° related to the diffuse reflection caused by the fibril network [40,41]. In addition, all groups exhibited a high water absorption capacity and neutral pH (Fig. S5A, **B**, Supporting **Information**). Notably, SDS−PAGE analysis indicated that the components of dECM remained essentially unchanged throughout the freeze-thaw treatments (Fig. S5C, Supporting **Information**).

Good biocompatibility is a prerequisite for tissue-engineering biomaterials. In this study, RAW 264.7 macrophages and fibroblasts were respectively seeded on the dECM, and a CCK-8 assay was performed to evaluate cell proliferation. Compared to the control, the cell vitality of F/T 3 and F/T 7 significantly increased on day 3 (Fig. 1H). Freeze-thaw treatment can efficiently remove the cellular composition and reduce the foreign body reaction by forming intracellular ice crystals and causing cell lysis, but overuse of freeze-thaw treatments may lead to the structural impairment and exposure of the secondary conformation of

collagen fibrils causes severe adverse immune responses [34]. Three freeze-thaw cycles might be adequate to remove the cells while maximally preserving the ECM proteins and native matrix structure in our decellularization protocol. Furthermore, the rat subcutaneous model was used to evaluate the system toxicity of dECM. Four 10 mm × 10 mm square pieces of dECM from the same group were implanted, and all rats remained healthy. No complications, such as infection, wound dehiscence or delayed wound healing was observed throughout the study. Considering that dECM completely degraded in a month, the health state of important organs was examined on day 28. No lesions were observed in the major organs in any of the three groups (Fig. S6, Supporting **Information**). The dECM-derived biomaterials exhibited good biocompatibility due to the preserved native 3D biological structure and bioactive composition of the dECM [6].

The degradability of dECM was investigated *in vitro* using matrix metalloproteinase-1 (MMP-1), the predominant collagenase that cleaves collagen type I and III [42]. Over 90% of the dECM in the control had already been degraded, while 20% of dECM in F/T 3 remained undissolved in 48 h (Fig. 1I). This demonstrated that the extracellular biodegradation behavior of dECM could be prolonged by freeze-thaw treatment.

These results indicated that the dECM in all three groups was cell-free and maintained the conformation and structure of collagen, and showed good biocompatibility and biodegradability. Consistent with previous studies, ECM ultrastructure was relatively well preserved during freeze-thaw treatments [32,43]. This may create an optimized cellular microenvironment conducive to the growth of 3D structured tissue, further contributing to better biocompatibility [44].

2.2. Freeze-thaw treatment imparts tunability to multiscale mechanical properties of dECM

The mechanical properties of the dECM across multiple length scales are critical to its clinical performance as the mechanical cues shape our tissue responses to the biomaterials [31]. The macroscale mechanical properties of biomaterials determine their operating characteristics and interaction with organs or tissues, while microscale ones direct cellular responses, and nanoscale mechanical properties influence *in situ* molecular interactions [45].

2.2.1. The structure of dECM

To investigate the impacts of freeze-thaw treatment on the structure of dECM, we characterized its surface morphology and pore size distribution. The dECM membrane contained a compact layer and rough layer (Fig. 2A and Fig. S7, Supporting Information). Quantification analysis of scanning electron microscopy (SEM) images indicated that the average pore size of dECM decreased significantly from 10 mm to 5 mm after undergoing 7 freeze-thaw cycles. Moreover, the collagen diameter of dECM in the F/T 7 group was found to be only half of that in the Con group. The pore size of the network and the diameter of collagen bundles decreased with an increase in the number of freeze-thaw cycles, which was further confirmed by mercury intrusion porosimetry (MIP) in a dry state and atomic force microscopy (AFM) under physiological conditions (Fig. 2A–E). Similar structural alterations resulting from the exfoliation of collagen fibrils associated with water-ice phase change during freeze-thaw treatment have been reported in previous studies [30,46].

2.2.2. The macro-mechanical properties of dECM

The uniaxial tensile test is commonly used to study the mechanical properties at the macroscale of the collagen membrane, assessing the operational performance of the dECM [47–49]. The dECM exhibited nonlinear elasticity with an approximately exponential relationship between stress and strain (Fig. 2H). The macroscopic stiffness and ultimate tensile strength were significantly enhanced, while the strain was reduced after three freeze-thaw cycles (Fig. 2I, J and K). The deformation process of dECM in tensile tests involves four regions: the toe region, heel region, elastic region, and failure [50,51]. All three groups performed similarly in the toe region, implying that the stress used to remove the macroscopic crimps was the same. Kink strengthening occurred earlier in the dECM of F/T 3, accounting for a lower failure strain in the F/T 3 group. Furthermore, more energy was needed to stretch the kinks and unlock the triple helix structure in the elastic region in the F/T 3 group (Fig. 2F). We speculated that freeze-thaw treatment altered the elastic modulus of dECM by affecting dECM at the collagen fiber level at the microscopic scale.

2.2.3. The nano- and micro-mechanical properties of dECM

AFM is a powerful technique that provides both structural and mechanical information with high precision under physiological conditions ranging from kPa to GPa. The nanomechanical properties were evaluated via AFM using pyramidal tips to provide both structural and mechanical information under physiological conditions (Fig. 3A). The elastic modulus of collagen fiber networks of dECM in the control, F/T 3, and F/T 7 were 0.56, 0.76, and 0.95 MPa, respectively, showing an improvement with an increasing number of freeze-thaw cycles (Fig. 3B and C). To focus on the individual collagen fibrils instead of the whole membrane, we performed AFM measurements in a finer range and found that the elastic modulus of collagen fibrils increased with an increasing number of freeze-thaw cycles (Fig. 3D and E). Although seven freeze-thaw cycles yield a higher nanoelastic modulus of individual collagen fiber (reflected by AFM nanoindentation using pyramidal tips) than that achieved by three freeze-thaw cycles, the macro- and micro-elastic modulus of dECM were intriguingly decreased with more freeze-thaw cycles involved. It is worth noting that the overall mechanical property of the dECM is determined not only by the elastic modulus of individual collagen fibrils but also the structure of the collagen network, which is also influenced by the freeze-thaw cycles. We showed seven cycles of freeze-thaw treatment led to a significant reduction in the pore size of dECM, suggesting the formation of a more densified collagen network. This is responsible for the decrease in the overall elastic modulus in this group. Therefore, the optimal cycles of freeze-thaw treatment need to be explored to achieve ideal elastic modulus of individual collagen fibril without compromising the overall structure of the collagen network.

Further, we performed finite element analysis (FEA) to simulate the interplay between the collagen network and the pyramidal tips. As shown in Fig. 3F stress and deformation were concentrated on individual collagen fibers during detection by the pyramidal tips without disturbing the structure of collagen network. Although pyramidal tips allow higher spatial resolution detection, the microenvironment detected by spherical tips might be more similar to the stiffness sensed by the cells [52,53]. So, we used a spherical tip to measure the microelastic modulus of dECM (Fig. 4A, B, C). However, it was difficult to obtain a large amount of valid data, as the samples were not sufficiently flat and stably fixed to allow AFM measurements [54]. Cryosection is an ideal aid to overcome this obstacle, as it has little influence on the elastic modulus of the dECM [55]. Therefore, we exploited cryosection to obtain an accurate and efficient measurement of the micromechanical properties. The elastic modulus of the dECM slices in F/T 3 probed with spherical tips was higher than that of the other two groups (Fig. 4D and E). Notably, the results for pyramidal tips differed from those for spherical tips. In contrast, the contact area between the spherical tip and collagen network was much larger, suggesting that the measurement disturbed the collagen network structure, and deformation and stress changed in a larger region (Fig. 4F). These results verified that spherical tips could provide information on microscale stiffness and structure, indicating that spherical tips could better reflect what cell “feels” [52].

The hydration level shows a distinct effect on mechanical property of collagen based materials such as dECM [56]. The elastic modulus of dECM is at MPa-scale in the dry state, while in the wet state it can increase to GPa-scale [57]. This is explained by the fact that the collagen molecules in the dehydrated microfibril are initially mostly straightened

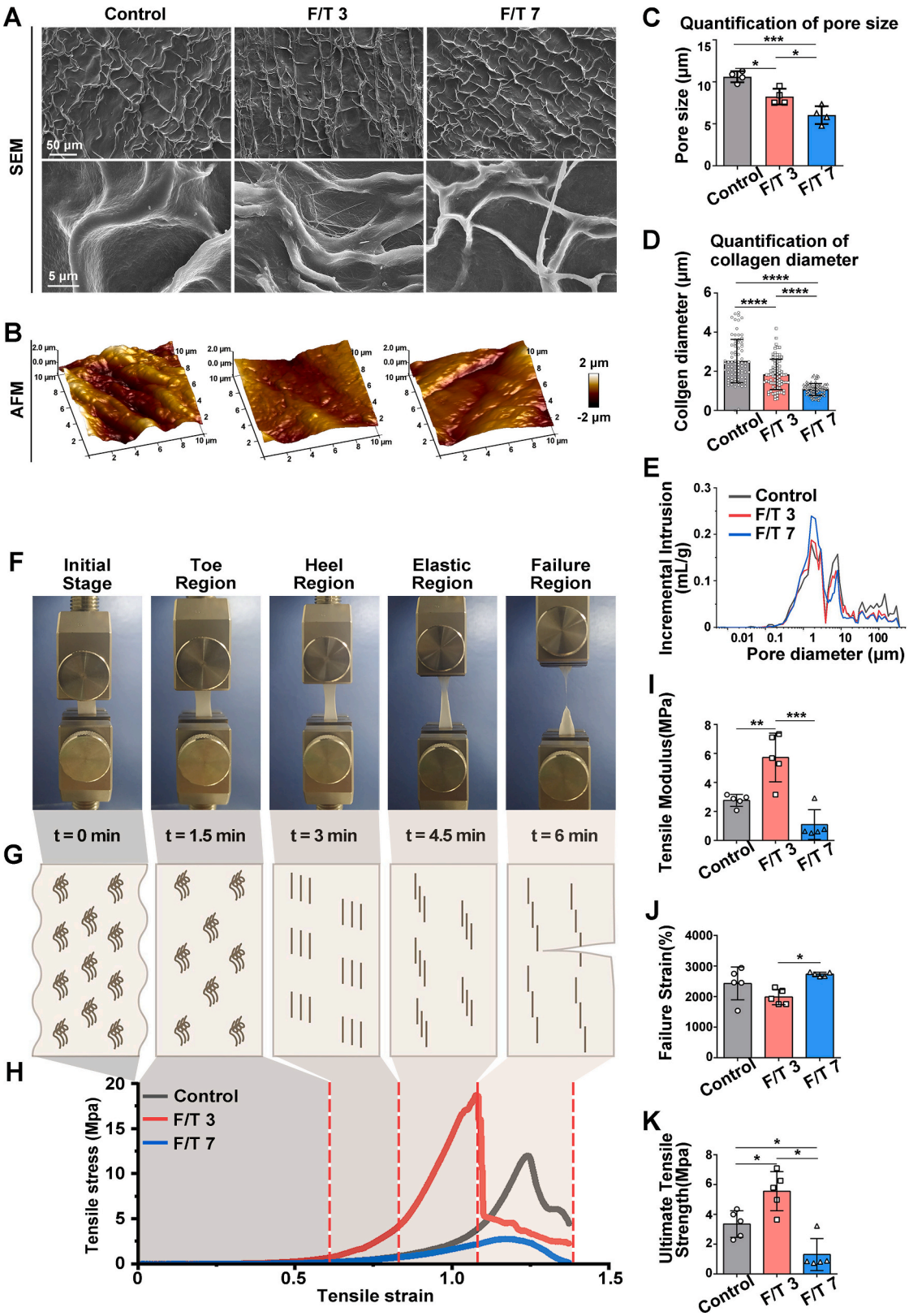

Fig. 2. The structure and macromechanical property of freeze-thaw treated dECM. (A and B) SEM (A) and AFM (B) images showing smooth surface morphologies of dECM in control, F/T 3, and F/T 7. **(C and D)** Quantification of pore size (C) and diameter of dECM (D) according to SEM (n = 3). **(E)** Differential pore volume distribution of control, F/T 3 and F/T 7 measured using mercury intrusion porosimetry. **(F and G)** Representative photographs (F) showed five distinct regions of dECM deformation during mechanical testing, with schematic illustrations depicting the collagen stretching process (G). **(H)** Representative stress-strain curves of control, F/T 3, and F/T 7. The tensile mechanical properties of dECM measured using a universal testing machine under physiological conditions. The deformation process of dECM in the tensile test involves four regions: toe region, a heel region, elastic region, and failure. **(I - K)** The tensile modulus (I), failure strain (J), and ultimate tensile strength (K) were measured.

Statistical analysis was performed using ANOVA and multiple comparisons post-hoc tests (Tukey HSD). $*p < 0.05$, $**p < 0.01$, $***p < 0.001$.

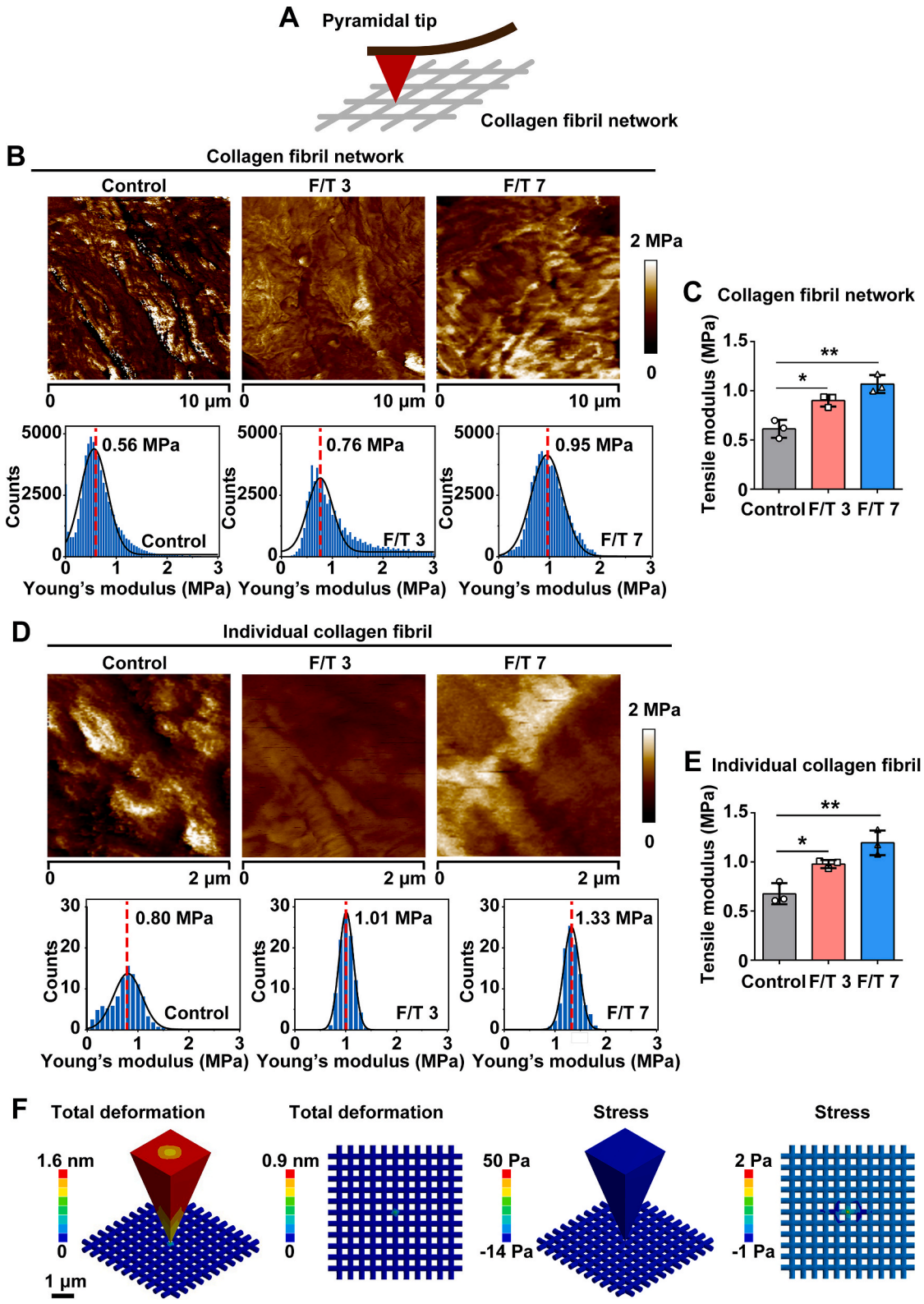

Fig. 3. Nanomechanical properties of dECM. (A) Schematic diagram showing the nanomechanical property of freeze-thaw treated dECM was detected by a pyramidal tip. **(B and D)** Representative force maps showing the nanomechanical property of the collagen fibril network (B) and individual collagen fibrils (D) measured by pyramidal tips, indicating the rise of elastic modulus at nanoscale with the increasing freeze-thaw cycles. The histogram of the elastic modulus for each force map is shown below. Gauss distribution fits (represented by black solid curves) were conducted to evaluate the elastic modulus. The abscissa of the peaks represents the elastic modulus of the area. **(C and E)** Young's modulus of collagen fibril network (C) and individual collagen fibril (E) was detected using pyramidal tips indicating freeze-thaw treatment enhance the elastic modulus at nanoscale. **(F)** 3D Finite element simulation of a pyramidal tip indenting the collagen fiber network, indicating that the deformation and stress were limited in individual collagen fibril.
Statistical analysis was performed using ANOVA and multiple comparisons post-hoc tests (Tukey HSD). $*p < 0.05$, $**p < 0.01$.

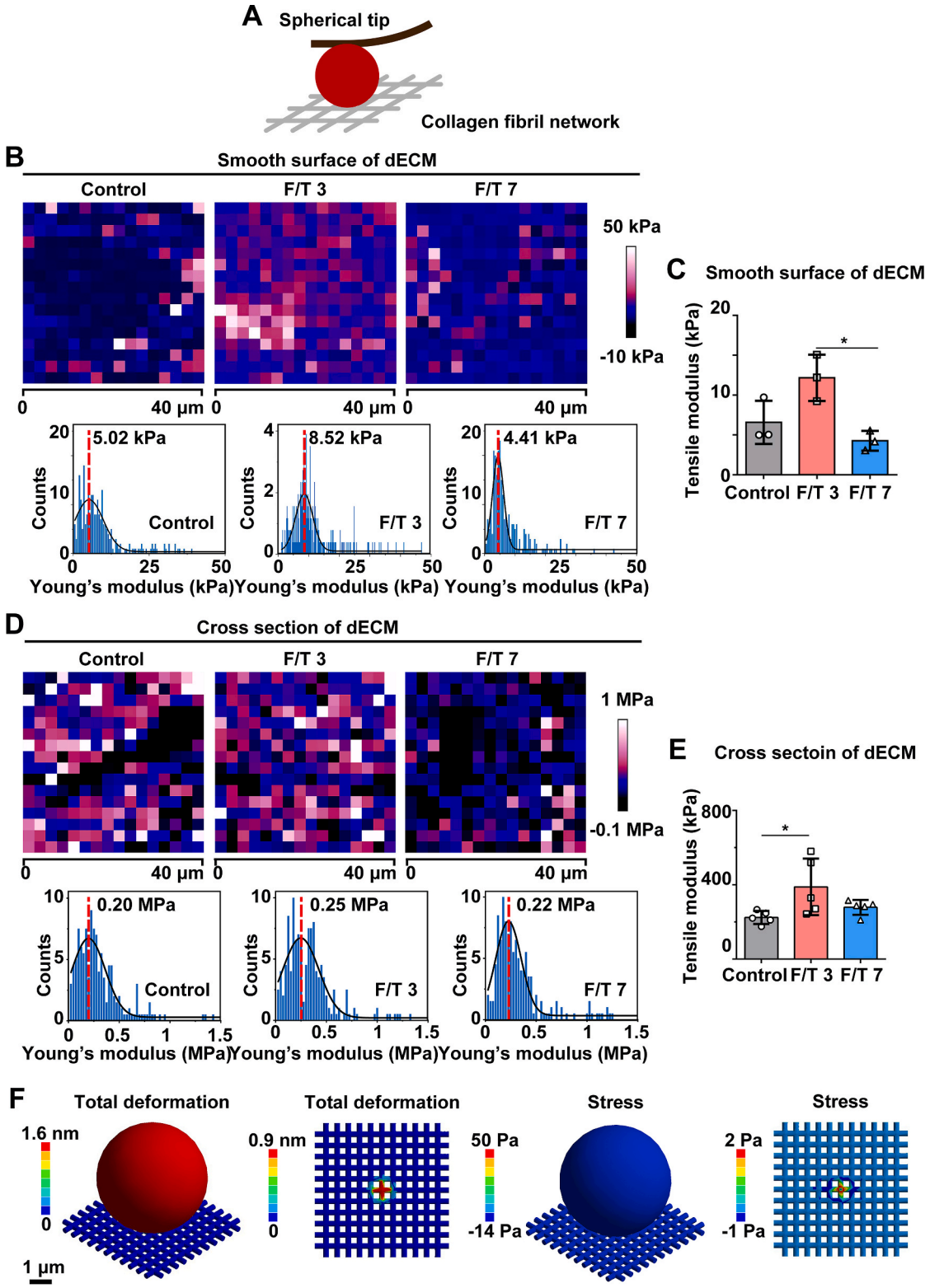

Fig. 4. Micromechanical properties of dECM. (A) Schematic diagram showing the micromechanical property of freeze-thaw treated dECM was detected by a spherical tip. **(B and D)** Representative force maps showing the micromechanical property of the smooth surface (B) and cross section (D) of dECM by spherical tips. The cross sections of dECM were prepared by cryosection. The histogram of the elastic modulus for each force map is shown below. Gauss distribution fits (represented by black solid curves) were conducted to evaluate the elastic modulus. The abscissa of the peaks represents the elastic modulus of the area. **(C and E)** Young's modulus of smooth surface (C) and cross sections (E) of dECM was detected using spherical tips, indicating three freeze-thaw cycles contribute to the highest elastic modulus at microscale. **(F)** 3D Finite element simulation of a spherical tip indenting the collagen fiber network, indicating that spherical tips could better reflect mechanosensation of cells.

Statistical analysis was performed using ANOVA and multiple comparisons post-hoc tests (Tukey HSD). $^{*}p < 0.05$.

during the deformation process rather than stretched [58]. Therefore, it is critical to evaluate the mechanical property of collagen based materials under fully hydrated conditions to ensure physiologically relevant results [59].

The effect of freeze-thaw treatment on collagen-based materials is associated with the coldest setpoint temperature, cooling rate, freezing hold time, thawing media, and number of cycles [46,60,61]. In our study, we found that freeze-thaw treatment decreased the diameter and enhanced the stiffness of collagen fibers, and the stiffness increased with the increase in the number of free-thaw cycles. This indicates that a certain number of freeze-thaw cycles could enhance the mechanical properties of dECM, above which they may lead to structural impairment and mechanical property regression. Collectively, freeze-thaw treatment could be an effective approach for fabricating mechanically tunable dECM.

2.3. Freeze-thaw treated dECM modulates macrophage polarization in vitro

Given the significant role of mechanical properties in determining macrophage responses, RNA sequencing (RNA-seq) was used to analyze the changes in macrophage gene expression activated by freeze-thaw-treated dECM [62–64]. The specimen showed good stability according to the correlation analysis ($R^2 > 0.95$) (Fig. S9A, Supporting **Information**). The heatmap, Venn diagram, and volcano plots show a wide range of gene expression differences among the three groups (Fig. 5A, and Figs. S9B, C, D, E, Supporting **Information**). Principal component analysis revealed that the F/T 3 group was significantly different from the control and F/T 7 groups, which might result from the distinguished micromechanical properties of the F/T 3 group compared with the control and F/T 7 groups, indicating that spherical tips could better reflect what cell "feels" than pyramidal tips (Fig. 5B) [53].

Subsequently, to explore the differences in macrophage response, we performed Gene Ontology (GO) enrichment analysis and Kyoto Encyclopedia of Genes and Genomes (KEGG) functional pathway analysis using Gene Set Enrichment Analysis (GSEA). The top 16 down-GO terms showed that the immune response was the major downregulated event compared with the control (Fig. 5C). Compared with the control, cytokine-cytokine receptor interaction and NF-κB signaling pathway were downregulated in F/T 3 and F/T 7, demonstrated to be associated with M1-like polarization (Fig. 5D, and Fig. S10A, Supporting **Information**) [65,66]. These data agree with previously reported studies in which the NF-κB signaling pathway, enhanced by Piezo type mechanosensitive ion channel component 1 (Piezo1) activity, mediated stiffness-dependent macrophage inflammatory activation [19]. However, it was interesting to note that the cell adhesion behavior-related terms, such as regulation of actin cytoskeleton, adherens and tight junctions and focal adhesion were upregulated in F/T 3, while cell adhesion molecules (CAMs) were downregulated in F/T 7 (Figs. S10B, C, D, E, Supporting **Information**). These findings implied that the dECM in F/T 3 and F/T 7 played opposite roles in cell adhesion. Furthermore, we analyzed the differentially expressed genes in F/T 3 group, finding that the response to stress related genes directly affect the immune response (Fig. 5E). Then, we focused on the differences in mechanotransduction and macrophage polarization related gene expression (Fig. 5F). The resulting heatmaps showed that dECM in F/T 3 significantly promoted cell adhesion and polarized macrophages toward an anti-inflammatory phenotype over a pro-inflammatory one. Additionally, accumulating evidence has verified that integrin and cadherin adhesion complexes perform important functions in sensing mechanical cues across multiple scales and transducing them into biological signals to mediate multiple cellular behaviors. Adhesion complexes (such as integrin and cadherin) and ion channels (including TRPV4 and PIEZO family) serve as mechanosensors that transmit mechanical forces inside the cell, transforming them into biochemical signals that regulate intracellular processes [64,67–69]. Based on the above analysis, we speculated that the NF-κB signaling pathway involved in macrophage mechanosensing in this study and freeze-thaw treatment modified macrophage polarization by promoting cell adhesion.

2.4. Freeze-thaw treated dECM exhibited good biocompatibility, controllable biodegradation, and ability to regulate macrophage polarization

To further investigate biocompatibility, biodegradation rate, and immune regulatory effects *in vivo*, a mechanically tunable dECM was implanted into a rat subcutaneous model [62,70].

2.4.1. The local biocompatibility, biodegradation, and integration capability of freeze-thaw treated dECM

Foreign body reaction (FBR)—the formation of foreign body giant cells (FBGCs) and fibrosis—can limit implant function and even lead to its ultimate failure [71–73]. The materials were implanted subcutaneously in rats and histologically analyzed 7, 14, and 28 days post-implantation to assess the foreign body reaction (Fig. 6A). Histological staining showed an inflammatory response band around the dECM, indicating a slight FBR to the biomaterials (Fig. 6B and Fig. S12, Supporting **Information**). On day 7, a few FBGCs were observed at the interface between the dECM and the periphery (Fig. 6D). No significant differences were observed in the integration rate among the three groups (Fig. 6E). On day 14, fewer FBGCs were observed, and the capsule thickness of F/T 3 was the thinnest, implying a minor FBR in the local tissue (Fig. 6C, G). The inflammation reaction scores implied that these dECM exhibited better biocompatibility than the controls (Fig. 6F, Table S1, Supporting **Information**).

The degradation rate of F/T 3 was the slowest, which may be partly responsible for the prolonged degradation time, according to the current knowledge that FBGCs could degrade collagen-based biomaterials by phagocytosis (Fig. 6B) [74]. Non-cross-linked dECM generally starts to disintegrate on day 14 and is almost completely degraded within a month, which is in line with previous results [74,75]. The main disadvantages of collagen-based biomaterials are poor mechanical properties and rapid biodegradation [76]. Freeze-thaw treatment ameliorated the degradation of dECM while improving its mechanical properties.

2.4.2. The ability of freeze-thaw treated dECM to regulate macrophage polarization

As previously mentioned, macrophage polarization can be modulated by manipulating the mechanical properties of dECM [62]. To verify the effect of macrophages on dECM, immunohistochemical staining was performed on the dorsal skin of rats implanted with control, F/T 3, and F/T 7 on days 7 and 14. Fig. 7A and B showed that infiltration of $CD68^+$ macrophages was observed in all three groups, and the major $CD68^+$ macrophages were distributed at the junction of the dECM and soft tissue (Fig. S14, Supporting **Information**). Quantitative analysis of immunohistochemical staining showed that there were fewer M1 macrophages ($iNOS^+$) on the smooth surface of the F/T 3 group on day 7 and more M2 macrophages ($CD163^+$ and/or $CD206^+$) on days 7 and 14 (Fig. 7B, D) compared with the control group [8].

The ability of dECM to induce macrophage polarization *in vitro* was verified using reverse transcription-quantitative polymerase chain reaction (RT-qPCR) (Fig. 7E). After dECM were co-cultured with macrophages for 24 h, the expression of M1-like macrophage marker genes, including CD86, CD11c, and TNFα was significantly reduced by dECM from F/T 7, in contrast to the control, while the expression of M2 macrophage marker genes including CD163, CD206, and ARG was significantly elevated by dECM from F/T 3 compared with the control and F/T 7 groups. These findings verified the *in vivo* observations that F/T 3 could induce an anti-inflammatory macrophage phenotype. Therefore, we can infer that freeze-thaw treatment might impart dECM with the ability to induce M2-like macrophage polarization.

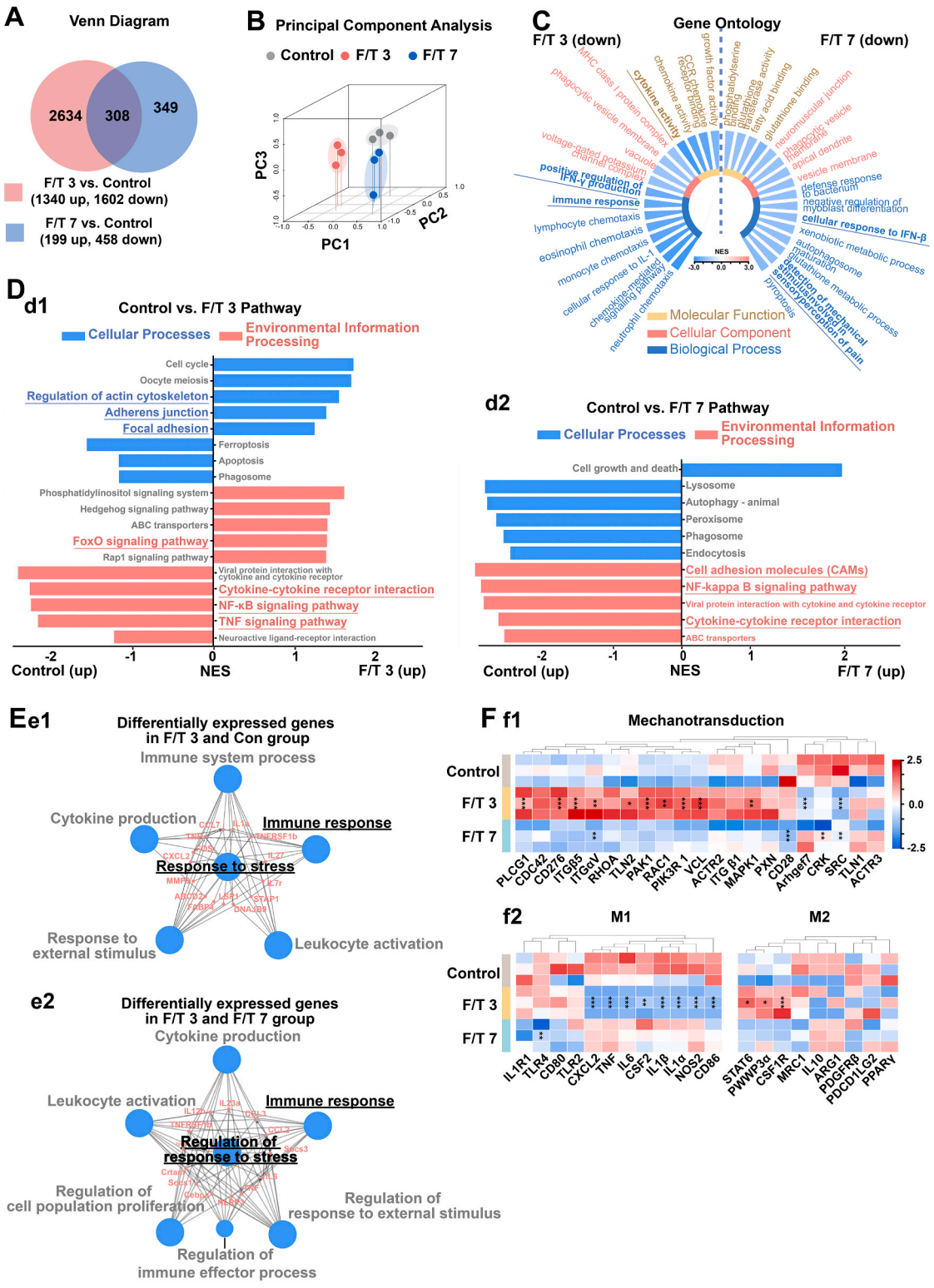

Fig. 5. Freeze-thaw treated dECM elicit mechanotransduction to polarize macrophages. (A and B) Venn diagram (A) and principal component analysis (B) of macrophage response to dECM treated with different number of freeze-thaw cycles, indicating a larger difference between the F/T 3 group and the other two groups. **(C)** The top eight down-GO terms in biological process, four in cellular component and four in molecular functions, demonstrating the immune response is the major downregulated event in F/T 3 group. **(D)** Top five up- and down-KEGG terms in cellular processes and environmental information processing in F/T 3 (d1) and F/T 7 (d2). Immune response and mechanotransduction related events are highlighted by increasing font size and underlining. **(E)** The functional enrichment analysis of F/T 3 vs Control (e1) and F/T 3 vs F/T 7 (e2), showing the direct interaction of immune response and mechanotransduction. **(F)** Heatmap analysis of expressed genes in mechanotransduction (f1) and macrophage polarization (f2).

Statistical analysis was performed using ANOVA and multiple comparisons post-hoc tests (Tukey HSD). $*p < 0.05$, $**p < 0.01$, and $***p < 0.001$.

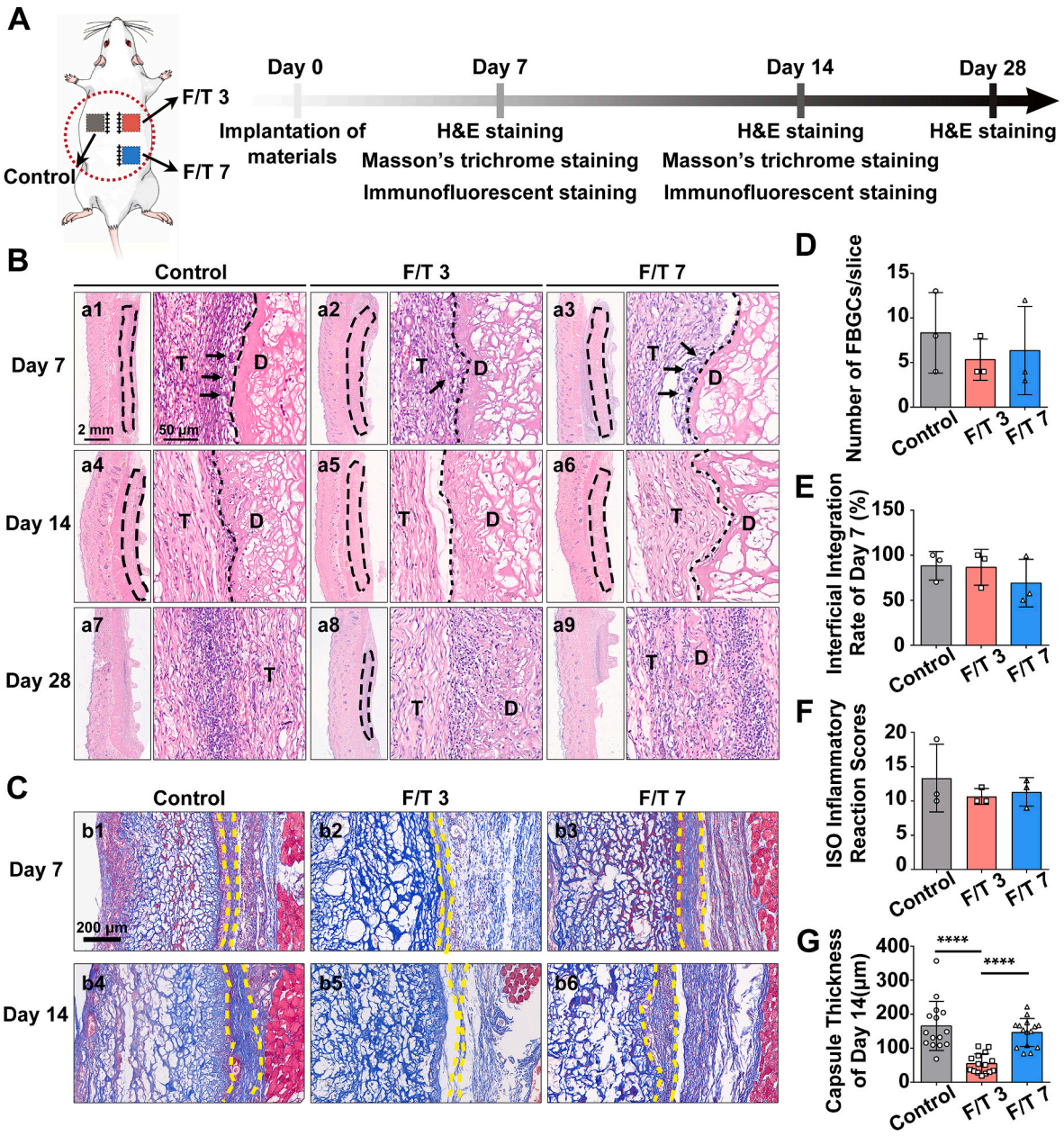

Fig. 6. Biocompatibility and biodegradability of freeze-thaw treated dECM *in vivo*. **(A)** Workflow for evaluating the biocompatibility and biodegradability of dECM in a rat subcutaneous model. **(B)** H&E staining sections of subcutaneously implanted samples in control, F/T 3, and F/T 7 groups at days 7, 14, and 28. Black dashed lines, the margin of dECM; T, the tissue region; D, the degrading materials; black arrows, FBGCs. **(C)** Representative histological images of subcutaneous injury using Masson's Trichrome staining. The yellow dashed lines mark the margin of fibrous capsule. **(D)** The number of FBGCs per slice indicating the severity of FBR. **(E)** Semiquantitative analysis of average integration rate of smooth surfaces. **(F)** Score of inflammatory reaction of dECM according to ISO 10993-6:2016. **(G)** Characterization of the thickness of the fibrous capsule using image analysis.
Statistical analysis was performed using ANOVA and multiple comparisons post-hoc tests (Tukey HSD). $*p < 0.05$, $**p < 0.01$, $***p < 0.001$, and $***p < 0.0001$.

2.5. Freeze-thaw treated dECM accelerates wound healing in rats

To evaluate the progression of wound healing, dECM scaffolds of control, F/T 3, and F/T 7 were implanted in the Sprague Dawley (SD) rat wound healing model (Fig. 8A). The speed of wound healing was evaluated based on macroscopic wound closure (Fig. 8B and C). Quantification of relative wound area showed that freeze-thaw treated dECM was significantly more effective than the control in full-thickness skin regeneration, and the F/T 3 group showed the highest wound closure rate (Fig. 8D).

On day 5, the boundary between the dECM and native tissue was obvious, with the epithelial tongue attached to the dECM (Fig. 8F). On day 10, wounds were fully re-epithelialized in the F/T 3 and F/T 7 groups, and the dECM was integrated with the native tissue. On day 15, the wounds in F/T 3 were almost healed, and the dermis layer was regenerated with neogenic hair follicles developed in the skin. In contrast, fewer neogenic hair follicles and glands were observed in the control and F/T 7 groups. The gap width of the F/T 3 group was significantly shorter than that of the other two groups, probably due to the anti-inflammatory microenvironment (Fig. 8E) [77–79]. In particular, the inherent wound contraction in rat skin could only promote the closure of the epidermis but did not favor the maturation of the dermis, indicating that these neogenic tissues profited from freeze-thaw treated dECM [77]. To further distinguish dECM from regenerated tissue, Masson's

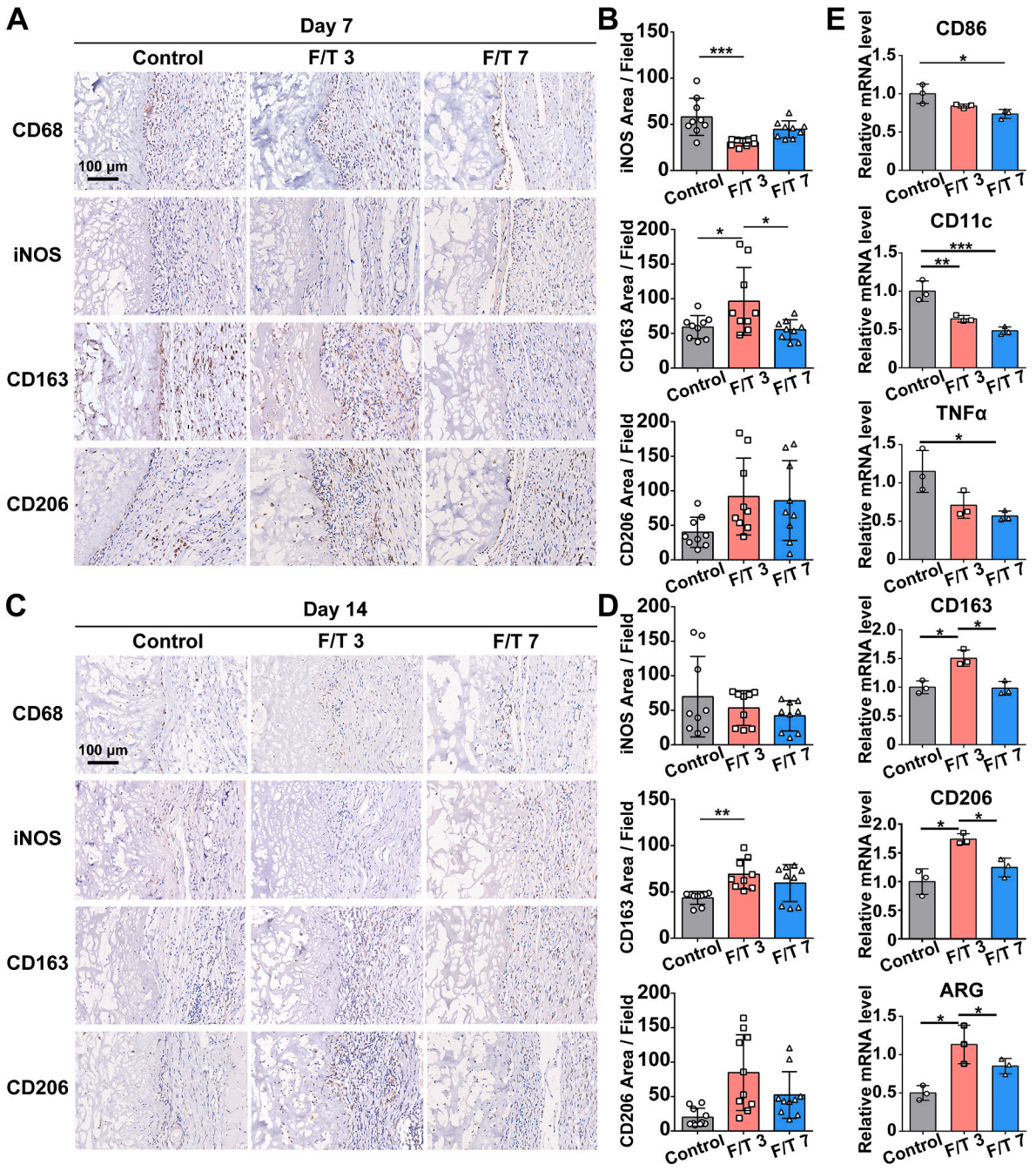

Fig. 7. The effect of freeze-thaw treatment on macrophage polarization. (A and C) Immunohistochemistry analysis showing the presence of $CD68^+$, $iNOS^+$, $CD163^+$ or $CD206^+$ macrophages at day 7 (A) and 14 (C). **(B and D)** Quantification for the expression of iNOS, CD163, and CD206 on day 7 (B) and day 14 (D). **(E)** The relative mRNA level of CD86, CD11c, TNF, CD163, CD206, and ARG of macrophages in the tested groups.
Statistical analysis was performed using ANOVA and multiple comparisons post-hoc tests (Tukey HSD). $^*p < 0.05$, $^{**}p < 0.01$, and $^{***}p < 0.001$.

trichrome staining was performed on day 15 (Fig. 8G). Notably, the dECM was not fully degraded and was located below the regenerated tissue, demonstrating that dECM treated with three freeze-thaw cycles could promote soft tissue regeneration instead of just working as a wounding dressing. Further, the wound healing rate with or without dECM in F/T 3 group were evaluated in 20 mm wound model in SD rats, and dECM did promote wound closure at the early stage (Fig. S15, Supporting **Information**). Regrettably, the silicone rings were broken in three days and wound without dECM showed evident contraction, which lead to a faster closure rate.

Compared with the dECM in other groups, the one produced with three freeze-thaw cycles possess a higher tensile modulus to around 6 MPa at macroscale. Meanwhile, its tensile modulus in microscale remains the highest among the three tested group, falling to a level of around 0.4 MPa. Additionally, the nanomechanical properties of F/T 3 is around 1 MPa, at a comparable level relative to F/T 7. In recent years, more and more evidence has suggested that it would be beneficial to tailor the mechanical property of the biomaterials to that of the target tissue [80,81]. Considering the tensile modulus of dorsal skin of rat to be around 1–10 MPa [82,83], it is not surprising that F/T 3 dECM bearing the most similar tensile modulus was found to contribute to the best biological outcome.

In addition, we performed immunofluorescence staining to investigate the role of macrophage polarization status induced by freeze-thaw

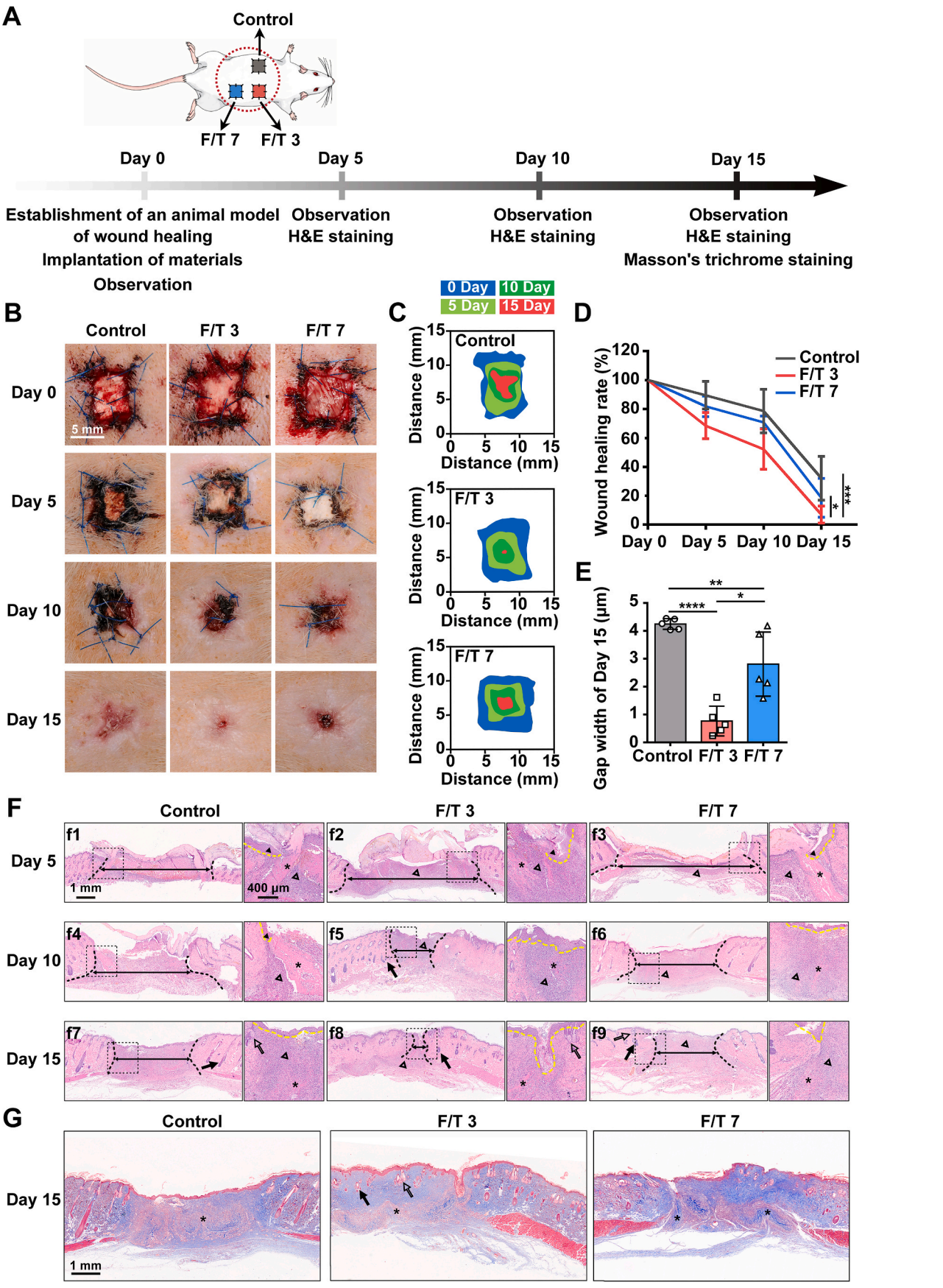

(caption on next page)

Fig. 8. The efficacy of freeze-thaw treated dECM in wound healing. (A) Workflow for evaluating the performance of dECM in a rat wound healing model (n = 6). **(B)** Representative images showing the wound closure at days 3 , 5, 10, and 15 (n = 6). **(C)** The schematic diagram of the dynamic wound healing process with a time range of 15 days (n = 6). **(D)** Quantitative data of relative wound area at days 3 , 5, 10, and 15 compared to that on day 0 in the three groups. n = 6 for each group. **(E)** Wound width quantification on day 15 (n = 5). **(F)** Representative H&E staining images at days 3 , 5, 10, and 15. Black dashed lines, wound edges; black triangle, granulation tissue; black lines, wound width; yellow dashed lines, the margin of epithelium; black arrows, hair follicle; white arrows, sebaceous gland; asterisks, residual dECM membrane (n = 5). **(G)** Representative images of Masson's trichrome staining at day 15. All graphs show mean ± standard deviation (n = 3). Statistical tools used: one-way ANOVA and multiple comparisons post-hoc tests (Tukey HSD). n = 6 for d, e, f. $*p < 0.05$, $**p < 0.01$, and $***p < 0.001$.

treated dECM in wound healing (Fig. 9A). On day 5, the number of $CD68^+iNOS^+$ cells was significantly lower in groups F/T 3 and F/T 7 compared with the control group, whereas the number of $CD68^+CD206^+$ cells was higher in group F/T 3, indicating that dECM in group F/T 3 promoted M2 rather than M1 polarization (Fig. 9B). These results aligned well with prior study on macrophage polarization in the rat subcutaneous model, suggesting that freeze-thaw treated dECM had a marked immunomodulatory effect on macrophage polarization in the process of wound healing.

In summary, a mechanically tunable dECM that preserved the native 3D biological structure was successfully fabricated using freeze-thaw treatment. The structure and mechanical properties of freeze-thaw treated dECM were modified across multiple length scales, imparting it good biocompatibility, biodegradation, and the ability to regulate macrophage polarization. In particular, the adhesion behavior of macrophages on the dECM may be a key event that modulates macrophage polarization. Finally, manipulation of the elastic modulus of the dECM by freeze-thaw treatment enhanced wound healing *in vivo* (Scheme 1).

Understanding the mechanical properties of dECM from the molecular (nano- and micro-mechanical properties) to the organ level (macromechanical properties) is essential for designing the mechanics of biomaterials. It should be noted that although the tensile modulus was used to represent the macroscopic mechanical properties of dECM in this study, the tensile test is inaccessible to completely mimic the clinical usage of dECM. The characterization of the micromechanical properties of dECM deserves further consideration. Additionally, the immunomodulatory mechanisms of mechanical cues have not been well explained. A thorough in-depth understanding of mechanotransduction requires further experimental validation, such as the effects of

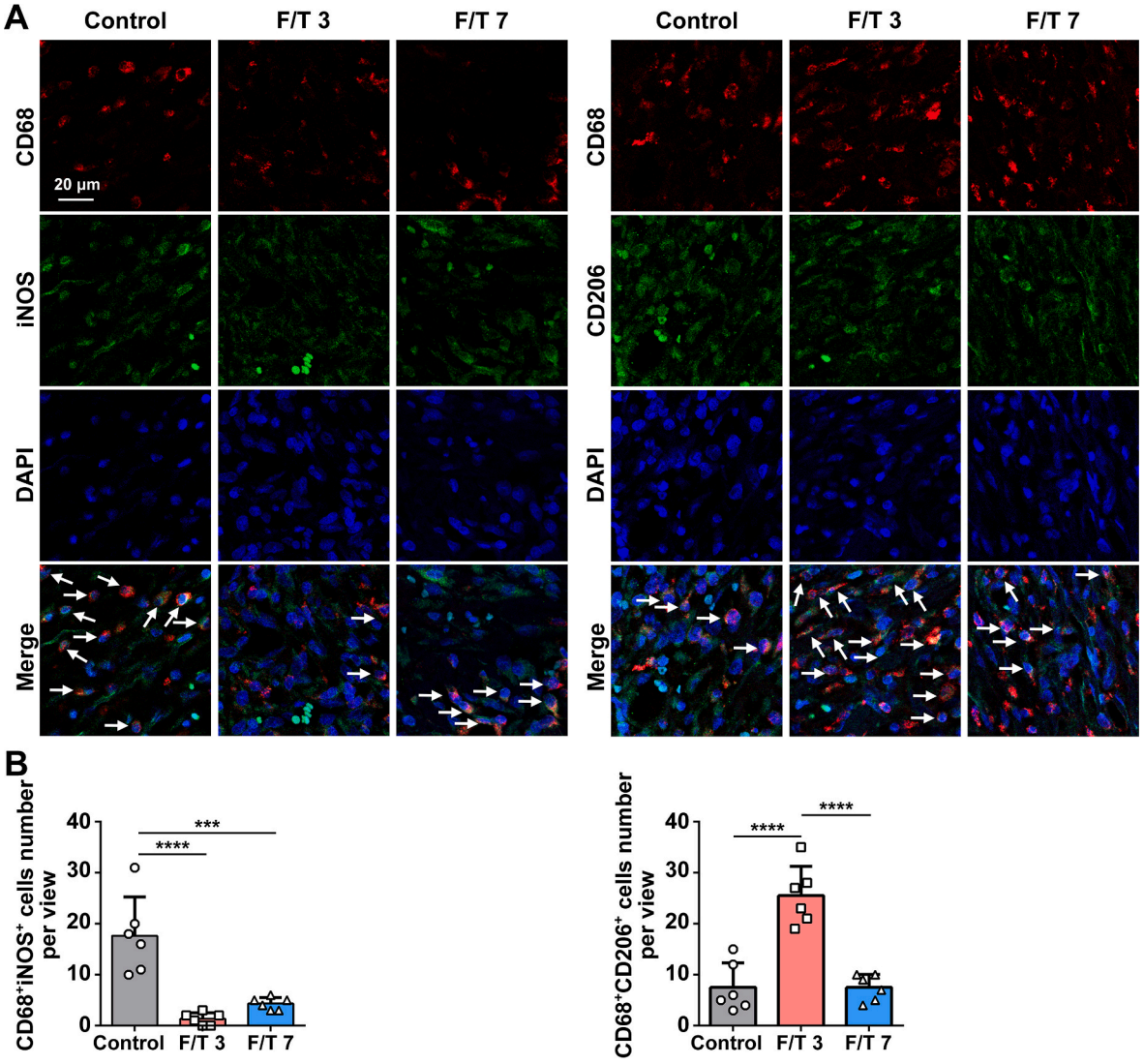

Fig. 9. The effect of freeze-thaw treatment on macrophage polarization in wound healing on day 5. (A) Representative images of $CD68^+iNOS^+$ (M1-like) and $CD68^+CD206^+$ (M2-like) immunostaining (n = 5). **(B)** Quantitative data of $CD68^+iNOS^+$ (M1-like) and $CD68^+CD206^+$ (M2-like) cells per field (n = 6).

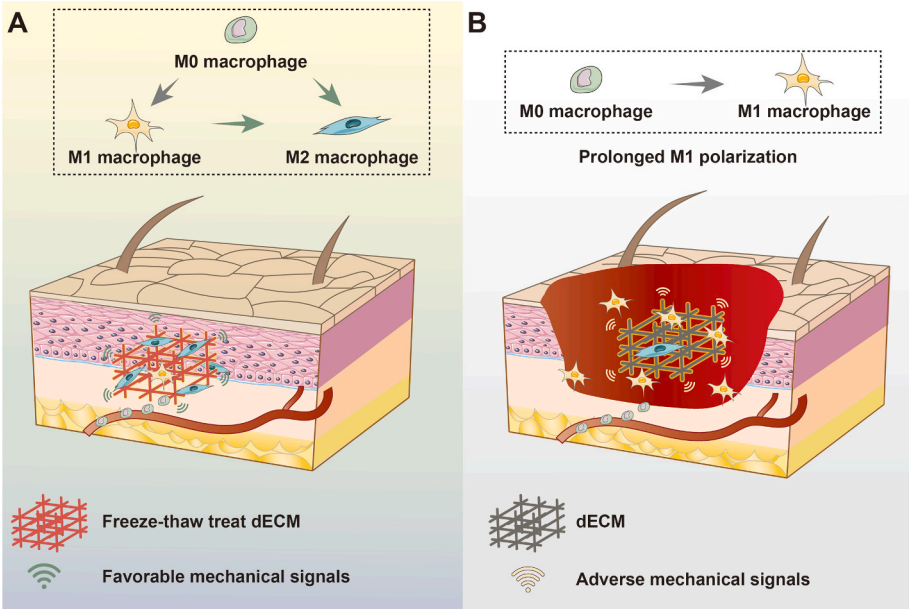

scheme 1. Schematic diagram. The dECM scaffolds designed and fabricated using a mechanics-immunomodulation-based strategy accelerate wound healing process. In brief, freeze-thaw treatment endows dECM with improved micromechanical property, which signals the M2 polarization of macrophage through mechanotransduction, leading to superior wound healing.

mechanical cues on cell adhesion behavior.

3. Conclusion

In this study, we report a potent mechanics-immunomodulation-based strategy for dECM development, which differs from traditional methods that rely on the addition of extrinsic chemicals or biological agents. We characterized the ultrastructure and elastic modulus of dECM from the molecular level to the length scale at which cell "feels" their environment. We show that the immunomodulatory property of dECM can be efficiently manipulated by tailoring its inherent micromechanical properties, leading to superior regenerative performance. We believe this mechanics-immune modulatory strategy may inspire the development of novel biomaterials for soft tissue regeneration.

4. Experimental section

4.1. Sample preparation

The porcine peritoneum was harvested from freshly slaughtered adult pigs and stored at −20 °C until use. The collected samples were dissected from the adjacent preperitoneal fat, subsequently cut into small pieces, and immersed in distilled water overnight at 4 °C. Then these pieces were frozen in liquid nitrogen for 5 min and thawed in distilled water at room temperature for 20 min, as a freeze-thaw cycle. The processed tissues were subjected to 0, 3 and 7 cycles (named Control, F/T 3 and F/T 7, respectively). After complete freeze-thaw treatment, the obtained samples were incubated 2 g/L sodium hydroxide solution at 4 °C for 12 h and transferred into 50%, 70%, 75%, 80%, 95%, 100% gradient ethanol, acetone and tert-butanol in order for dehydration. The processed product was degreased with N-hexane for 20 h, then acidified with 0.5% HCl for 5 h. After 20 g/L NaCl solution for hypertonic treatment at 4 °C for 5 h, the dECM membranes were treated with 10 g/L $NaHCO_3$ solution to adjust the pH to neutral. Between each step, the dECM membranes were thoroughly rinsed with distilled water. Finally, the dECM membranes were lyophilized and sterilized with 25 kGy of γ-irradiation. The macroscopic images of dECM were recorded by camera (Canon, Japan).

4.2. General characterization

The attenuated total reflectance Fourier transform infrared spectroscopy (FTIR), differential scanning calorimetry (DSC), X-ray diffraction (XRD), mercury intrusion porosimetry (MIP), scanning electron microscope (SEM), and energy dispersive spectroscopy (EDS) were used to investigate the physical and chemical characterization of dECM. These processes are described in detail in the Supporting **Information**.

4.3. Determination of multiscale mechanical properties

Tensile test was used to study the mechanical properties at the macroscale of dECM, while AFM was used to evaluate the nano-to-micro- mechanical property of dECM. The details are available in the Supporting **Information**.

4.4. In vitro cytocompatibility assay

The cytocompatibility of dECM was tested by cell counting kit-8 assay kit. The details are available in the Supporting **Information**.

4.5. In vitro biodegradation assay

The specimens (n = 3) were weighed, incubated in 2 ml of collagenase I (125 U/mg, Sigma, USA) solution (5 U/ml in phosphate-buffered saline (PBS)) at 37 °C, pH 7.4. After incubated for 12, 24, or 48 h, the samples were removed from incubation, washed with distilled water, and dried at 60 °C oven before weighing. The membrane degradations were represented as percentage the dry weight with respect to the initial dry weight.

$$\text{Retention mass} = M_t / M_0 \times 100\%$$

where M_0 is the original weight on day 0 and M_t is the weight at time point t.

4.6. RNA-seq and bioinformatic analysis

The detailed processes are described in the Supporting **Information**.

4.7. Surgical procedure

Subcutaneous model: All procedures were approved by the Institutional Animal Care and Use Committee of Sun Yat-Sen University (SYSU-IACUC-2021-000491). We purchased 200–300 g male SD rats from the Experimental Animal Center of Sun Yat-sen University and maintained them under pathogen-free conditions. A subcutaneous model was prepared as previously described [16]. Briefly, all rats underwent general anesthesia during the surgical procedure. The back of rats was shaved and disinfected with ethyl alcohol (75%). Lateral incisions were made on the back of the rats and dECM was implanted in each subcutaneous pocket. To evaluate the systemic toxicity of dECM, nine rats were randomly assigned to three groups, with each rat having four pieces of dECM (10 mm × 10 mm). After four weeks, the animals were sacrificed, and the heart, lung, liver, kidney, thymus, and brain tissues were obtained and fixed in 4% paraformaldehyde. A local biocompatibility test was performed according to ISO 10993-6:2016. These animals were euthanized 7, 14, and 28 days post-implantation for histological analysis.

Rat wound healing model: Eighteen male SD rats (4–8 weeks old, 250–400 g) were anesthetized, shaved, and disinfected, as described above. Full-thickness skin defects (6 mm × 6 mm) were generated on the backs of the rats. The dECM (10 mm × 10 mm) was then engrafted under the defect with the rough layer facing towards the tissue and secured to the surrounding tissue with 5–0 nonabsorbable surgical sutures. Wounds were recorded on days 0, 5, 10, and 15. The wound healing rate (WHR) was calculated as follows:

$$WHR = (S_0 - S_t) \ / S_0 \times 100\%$$

where S_0 is the wound area on day 0 and S_t is the wound area at time point t [84].

Histological and immunohistological assessment: Hematoxylin & Eosin (H&E) staining and Masson's trichrome staining were performed as described in dECM staining. IHC staining were performed for rabbit anti-CD68 (abcam, UK), rabbit anti-iNOS (abcam, UK), rabbit anti-CD163 (abcam, UK) and rabbit-anti CD206 (abcam, UK). The dewaxed slices were treated with heat-induced antigen retrieval and incubated in 3% H_2O_2 for 15 min. After blocked for 1 h with bovine serum albumin, the slices were incubated with CD68, iNOS, CD163 and CD206 antibodies(1 : 100, 1 : 100, 1 : 1000 , 1 : 5000, respectively) overnight at 4 °C, incubated with a goat anti-rabbit IgG secondary antibody (Gene Tech, China) and counterstained with hematoxylin for 1 min. Immunofluorescence staining were performed for mouse anti-CD68 (abcam, UK), rabbit anti-iNOS (abcam, UK), rabbit anti-CD206 (abcam, UK). In brief, the slides were dewaxed and washed with TBS for 5 min. After immersed in 3% H_2O_2 for 10 min and digested with protease for 20 min, the slices were blocked overnight. Following incubated with CD68, iNOS, and CD206 antibodies (1: 100, 1: 100, 1: 1000, respectively), the slides were washed in Tris-buffered saline with (TBST)-Tween 20 (TBST). The secondary antibodies were prepared with DAPI at 1:500,000 dilution. After incubation with prepared secondary antibody overnight, the slides were washed with Tris-buffered saline (TBS), mounted and stored at 4 °C before imaing.

4.8. Statistical analysis

Gauss distributions were fitted using Origin 2021b for AFM measurements. Immunofluorescence and wound area were quantified using Image-Pro Plus (v6.0.0.260, USA). The wound shape was recorded and stacked by Adobe Photoshop CC at different timepoint. Unpaired two-tailed Student's t-test was used to compare the means of two independent groups. Multiple comparisons post-hoc tests (one-way ANOVA for one independent variable or two-way ANOVA for two independent variables, Tukey HSD) were conducted using GraphPad Prism (version 6.01, CA), and $p < 0.05$ was considered statistically significant ($^*p < 0.05$; $^{**}p < 0.01$; $^{***}p < 0.001$; $^{****}p < 0.0001$).

Data availability statement

The data that support the findings of this study are available from the corresponding author upon reasonable request.

CRediT authorship contribution statement

Pu Luo: Methodology, Investigation, Formal analysis, Writing – original draft, Writing – review & editing. **Ruoxuan Huang:** Investigation, Formal analysis, Writing – original draft. **You Wu:** Investigation, Formal analysis, Writing – original draft. **Xingchen Liu:** Investigation, Formal analysis. **Zhengjie Shan:** Investigation, Formal analysis. **Li Gong:** Methodology, Investigation. **Shudan Deng:** Investigation. **Haiwen Liu:** Methodology, Investigation, Formal analysis. **Jinghan Fang:** Investigation, Formal analysis. **Shiyu Wu:** Methodology, Investigation. **Xiayi Wu:** Investigation. **Quan Liu:** Investigation. **Zetao Chen:** Investigation. **Kelvin W.K. Yeung:** Investigation. **Wei Qiao:** Conceptualization, Writing – original draft, Writing – review & editing, Supervision, Funding acquisition. **Shoucheng Chen:** Methodology, Investigation, Conceptualization, Methodology, Writing – original draft, Writing – review & editing, Supervision, Funding acquisition. **Zhuofan Chen:** Conceptualization, Writing – original draft, Writing – review & editing, Supervision, Funding acquisition.

Declaration of competing interest

The authors declare no conflict of interest.

Acknowledgements

This work was financially supported by National Natural Science Foundation of China (82071167, 82001095, 81970975, 81901055, 82201124, 82201119), China Postdoctoral Science Foundation (2021TQ0379, 2022M713575), Guangdong Basic and Applied Basic Research Foundation (2021A1515110380, 2023A1515011963), Health and Medical Research Fund (No.09201466), the Food and Health Bureau, the Government of the HKSAR, China.

Appendix A. Supplementary data

Supplementary data to this article can be found online at https://doi.org/10.1016/j.bioactmat.2023.05.011.

References

[1] S. Ellis, E.J. Lin, D. Tartar, Immunology of wound healing, Curr. Dermatol. Rep. 7 (2018) 350–358, https://doi.org/10.1007/s13671-018-0234-9.
[2] H. Xing, H. Lee, L. Luo, T.R. Kyriakides, Extracellular matrix-derived biomaterials in engineering cell function, Biotechnol. Adv. 42 (2020), 107421, https://doi.org/10.1016/j.biotechadv.2019.107421.
[3] L. Huleihel, G.S. Hussey, J.D. Naranjo, L. Zhang, J.L. Dziki, N.J. Turner, D.B. Stolz, S.F. Badylak, Matrix-bound nanovesicles within ECM bioscaffolds, Sci. Adv. 2 (2016), e1600502, https://doi.org/10.1126/sciadv.1600502.
[4] C. Wang, G. Li, K. Cui, Z. Chai, Z. Huang, Y. Liu, S. Chen, H. Huang, K. Zhang, Z. Han, Y. Li, G. Yu, Z.C. Han, N. Liu, Z. Li, Sulfated glycosaminoglycans in decellularized placenta matrix as critical regulators for cutaneous wound healing, Acta Biomater. 122 (2021) 199–210, https://doi.org/10.1016/j.actbio.2020.12.055.
[5] W. Han, N.K. Singh, J.J. Kim, H. Kim, B.S. Kim, J.Y. Park, J. Jang, D.W. Cho, Directed differential behaviors of multipotent adult stem cells from decellularized tissue/organ extracellular matrix bioinks, Biomaterials 224 (2019), 119496, https://doi.org/10.1016/j.biomaterials.2019.119496.
[6] X. Zhang, X. Chen, H. Hong, R. Hu, J. Liu, C. Liu, Decellularized extracellular matrix scaffolds: recent trends and emerging strategies in tissue engineering, Bioact. Mater. 10 (2022) 15–31, https://doi.org/10.1016/j.bioactmat.2021.09.014.
[7] D.S. Thoma, H.C. Lim, K.W. Paeng, M.J. Kim, R.E. Jung, C.H.F. Hammerle, U. W. Jung, Augmentation of keratinized tissue at tooth and implant sites by using autogenous grafts and collagen-based soft-tissue substitutes, J. Clin. Periodontol. 47 (2020) 64–71, https://doi.org/10.1111/jcpe.13194.

[8] R. Sridharan, A.R. Cameron, D.J. Kelly, C.J. Kearney, F.J. O'Brien, Biomaterial based modulation of macrophage polarization: a review and suggested design principles, Mater. Today 18 (2015) 313–325, https://doi.org/10.1016/j.mattod.2015.01.019.
[9] Z.T. Chen, T. Klein, R.Z. Murray, R. Crawford, J. Chang, C.T. Wu, Y. Xiao, Osteoimmunomodulation for the development of advanced bone biomaterials, Mater. Today 19 (2016) 304–321, https://doi.org/10.1016/j.mattod.2015.11.004.
[10] M. Rodrigues, N. Kosaric, C.A. Bonham, G.C. Gurtner, Wound healing: a cellular perspective, Physiol. Rev. 99 (2019) 665–706, https://doi.org/10.1152/physrev.00067.2017.
[11] R. Liu, S. Chen, P. Huang, G. Liu, P. Luo, Z. Li, Y. Xiao, Z. Chen, Z. Chen, Immunomodulation-based strategy for improving soft tissue and metal implant integration and its implications in the development of metal soft tissue materials, Adv. Funct. Mater. 30 (2020), 1910672, https://doi.org/10.1002/adfm.201910672.
[12] C. Hu, C. Chu, L. Liu, C. Wang, S. Jin, R. Yang, S. Rung, J. Li, Y. Qu, Y. Man, Dissecting the microenvironment around biosynthetic scaffolds in murine skin wound healing, Sci. Adv. 7 (2021), eabf0787, https://doi.org/10.1126/sciadv.abf0787.
[13] Y. Zhu, Z. Ma, L. Kong, Y. He, H.F. Chan, H. Li, Modulation of macrophages by bioactive glass/sodium alginate hydrogel is crucial in skin regeneration enhancement, Biomaterials 256 (2020), 120216, https://doi.org/10.1016/j.biomaterials.2020.120216.
[14] W.E.G. Müller, S. Wang, M. Ackermann, T. Gerich, M. Neufurth, M. Wiens, H. C. Schröder, X. Wang, Biologization of allogeneic bone grafts with polyphosphate: a route to a biomimetic periosteum, Adv. Funct. Mater. 29 (2019), 1905220, https://doi.org/10.1002/adfm.201905220.
[15] L. Pruett, C. Jenkins, N. Singh, K. Catallo, D. Griffin, Heparin microislands in microporous annealed particle scaffolds for accelerated diabetic wound healing, Adv. Funct. Mater. 31 (2021), 2104337, https://doi.org/10.1002/adfm.202104337.
[16] Y. Wu, S. Chen, P. Luo, S. Deng, Z. Shan, J. Fang, X. Liu, J. Xie, R. Liu, S. Wu, X. Wu, Z. Chen, K.W.K. Yeung, Q. Liu, Z. Chen, Optimizing the bio-degradability and biocompatibility of a biogenic collagen membrane through cross-linking and zinc-doped hydroxyapatite, Acta Biomater. 143 (2022) 159–172, https://doi.org/10.1016/j.actbio.2022.02.004.
[17] C.E. Chiang, Y.Q. Fang, C.T. Ho, M. Assuncao, S.J. Lin, Y.C. Wang, A. Blocki, C. C. Huang, Bioactive decellularized extracellular matrix derived from 3D stem cell spheroids under macromolecular crowding serves as a scaffold for tissue engineering, Adv. Healthc. Mater. 10 (2021), e2100024, https://doi.org/10.1002/adhm.202100024.
[18] R. Sridharan, B. Cavanagh, A.R. Cameron, D.J. Kelly, F.J. O'Brien, Material stiffness influences the polarization state, function and migration mode of macrophages, Acta Biomater. 89 (2019) 47–59, https://doi.org/10.1016/j.actbio.2019.02.048.
[19] H. Atcha, A. Jairaman, J.R. Holt, V.S. Meli, R.R. Nagalla, P.K. Veerasubramanian, K.T. Brumm, H.E. Lim, S. Othy, M.D. Cahalan, M.M. Pathak, W.F. Liu, Mechanically activated ion channel Piezo1 modulates macrophage polarization and stiffness sensing, Nat. Commun. 12 (2021) 3256, https://doi.org/10.1038/s41467-021-23482-5.
[20] H. Du, J.M. Bartleson, S. Butenko, V. Alonso, W.F. Liu, D.A. Winer, M.J. Butte, Tuning immunity through tissue mechanotransduction, Nat. Rev. Immunol. 23 (2023) 174–188, https://doi.org/10.1038/s41577-022-00761-w.
[21] J. Geng, Y. Shi, J. Zhang, B. Yang, P. Wang, W. Yuan, H. Zhao, J. Li, F. Qin, L. Hong, C. Xie, X. Deng, Y. Sun, C. Wu, L. Chen, D. Zhou, TLR4 signalling via Piezo1 engages and enhances the macrophage mediated host response during bacterial infection, Nat. Commun. 12 (2021) 3519, https://doi.org/10.1038/s41467-021-23683-y.
[22] H.C. Grillo, C.F. McKhann, The acceptance and evolution of dermal homografts freed of viable cells, Transplantation 2 (1964) 48–59, https://doi.org/10.1097/00007890-196401000-00006.
[23] T.W. Gilbert, T.L. Sellaro, S.F. Badylak, Decellularization of tissues and organs, Biomaterials 27 (2006) 3675–3683, https://doi.org/10.1016/j.biomaterials.2006.02.014.
[24] A.E.C. Granato, E.F. da Cruz, D.M. Rodrigues-Junior, A.C. Mosini, H. Ulrich, B.V. M. Rodrigues, A. Cheffer, M. Porcionatto, A novel decellularization method to produce brain scaffolds, Tissue, Cell 67 (2020), 101412, https://doi.org/10.1016/j.tice.2020.101412.
[25] J.Z. Yang, L.H. Qiu, S.H. Xiong, J.L. Dang, X.K. Rong, M.M. Hou, K. Wang, Z. Yu, C. G. Yi, Decellularized adipose matrix provides an inductive microenvironment for stem cells in tissue regeneration, World, J. Stem Cell. 12 (2020) 585–603, https://doi.org/10.4252/wjsc.v12.i7.585.
[26] N. Li, Y. Li, D. Gong, C. Xia, X. Liu, Z. Xu, Efficient decellularization for bovine pericardium with extracellular matrix preservation and good biocompatibility, Interact. Cardiovasc. Thorac. Surg. 26 (2018) 768–776, https://doi.org/10.1093/icvts/ivx416.
[27] J. Liao, B. Xu, R. Zhang, Y. Fan, H. Xie, X. Li, Applications of decellularized materials in tissue engineering: advantages, drawbacks and current improvements, and future perspectives, J. Mater. Chem. B 8 (2020) 10023–10049, https://doi.org/10.1039/d0tb01534b.
[28] H. Capella-Monsonis, D.I. Zeugolis, Decellularized xenografts in regenerative medicine: from processing to clinical application, Xenotransplantation 28 (2021), e12683, https://doi.org/10.1111/xen.12683.
[29] A. Ozcelikkale, B. Han, Thermal destabilization of collagen matrix hierarchical structure by freeze/thaw, PLoS One 11 (2016), e0146660, https://doi.org/10.1371/journal.pone.0146660.
[30] Y. Pei, K.E. Jordan, N. Xiang, R.N. Parker, X. Mu, L. Zhang, Z. Feng, Y. Chen, C. Li, C. Guo, K. Tang, D.L. Kaplan, Liquid-exfoliated mesostructured collagen from the bovine achilles tendon as building blocks of collagen membranes, ACS Appl. Mater. Interfaces 13 (2021) 3186–3198, https://doi.org/10.1021/acsami.0c20330.
[31] I. Jorba, J.J. Uriarte, N. Campillo, R. Farre, D. Navajas, Probing micromechanical properties of the extracellular matrix of soft tissues by atomic force microscopy, J. Cell. Physiol. 232 (2017) 19–26, https://doi.org/10.1002/jcp.25420.
[32] J. Fernández-Pérez, M. Ahearne, The impact of decellularization methods on extracellular matrix derived hydrogels, Sci. Rep. 9 (2019) 1–12, https://doi.org/10.1038/s41598-019-49575-2.
[33] Y. Kang, J. Chang, Channels in a porous scaffold: a new player for vascularization, Regen. Med. 13 (2018) 705–715, https://doi.org/10.2217/rme-2018-0022.
[34] J. Chakraborty, S. Roy, S. Ghosh, Regulation of decellularized matrix mediated immune response, Biomater. Sci. 8 (2020) 1194–1215, https://doi.org/10.1039/c9bm01780a.
[35] K. Kar, P. Amin, M.A. Bryan, A.V. Persikov, A. Mohs, Y.-H. Wang, B. Brodsky, Self-association of collagen triple helic peptides into higher order structures, J. Biol. Chem. 281 (2006) 33283–33290, https://doi.org/10.1074/jbc.M605747200.
[36] K. Kar, S. Ibrar, V. Nanda, T.M. Getz, S.P. Kunapuli, B. Brodsky, Aromatic interactions promote self-association of collagen triple-helical peptides to higher-order structures, Biochemistry 48 (2009) 7959–7968, https://doi.org/10.1021/bi900496m.
[37] X. Liu, N. Dan, W. Dan, Preparation and characterization of an advanced collagen aggregate from porcine acellular dermal matrix, Int. J. Biol. Macromol. 88 (2016) 179–188, https://doi.org/10.1016/j.ijbiomac.2016.03.066.
[38] Y. Li, Y. Li, Z. Du, G. Li, Comparison of dynamic denaturation temperature of collagen with its static denaturation temperature and the configuration characteristics in collagen denaturation processes, Thermochim. Acta 469 (2008) 71–76, https://doi.org/10.1016/j.tca.2008.01.006.
[39] T. Riaz, R. Zeeshan, F. Zarif, K. Ilyas, N. Muhammad, S.Z. Safi, A. Rahim, S.A. Rizvi, I.U. Rehman, FTIR analysis of natural and synthetic collagen, Appl. Spectrosc. Rev. 53 (2018) 703–746, https://doi.org/10.1080/05704928.2018.1426595.
[40] M. Andonegi, A. Irastorza, A. Izeta, K. de la Caba, P. Guerrero, Physicochemical and biological performance of aloe vera-incorporated native collagen films, Pharmaceutics 12 (2020) 1173, https://doi.org/10.3390/pharmaceutics12121173.
[41] S. Cheng, W. Wang, Y. Li, G. Gao, K. Zhang, J. Zhou, Z. Wu, Cross-linking and film-forming properties of transglutaminase-modified collagen fibers tailored by denaturation temperature, Food Chem. 271 (2019) 527–535, https://doi.org/10.1016/j.foodchem.2018.07.223.
[42] S. Sprangers, V. Everts, Molecular pathways of cell-mediated degradation of fibrillar collagen, Matrix Biol. 75–76 (2019) 190–200, https://doi.org/10.1016/j.matbio.2017.11.008.
[43] H. Amirazad, M. Dadashpour, N. Zarghami, Application of decellularized bone matrix as a bioscaffold in bone tissue engineering, J. Biol. Eng. 16 (2022) 1, https://doi.org/10.1186/s13036-021-00282-5.
[44] T.G. Kim, H. Shin, D.W. Lim, Biomimetic scaffolds for tissue engineering, Adv. Funct. Mater. 22 (2012) 2446–2468, https://doi.org/10.1002/adfm.201103083.
[45] J. Leijten, A. Khademhosseini, From nano to macro: multiscale materials for improved stem cell culturing and analysis, Cell Stem Cell 18 (2016) 20–24, https://doi.org/10.1016/j.stem.2015.12.013.
[46] M. Ekiert, J. Karbowniczek, U. Stachewicz, A. Mlyniec, The effect of multiple freeze-thaw cycles on the viscoelastic properties and microstructure of bovine superficial digital flexor tendon, J. Mech. Behav. Biomed. Mater. 120 (2021), 104582, https://doi.org/10.1016/j.jmbbm.2021.104582.
[47] S. Yang, X. Shi, X. Li, J. Wang, Y. Wang, Y. Luo, Oriented collagen fiber membranes formed through counter-rotating extrusion and their application in tendon regeneration, Biomaterials 207 (2019) 61–75, https://doi.org/10.1016/j.biomaterials.2019.03.041.
[48] J.J. Ahn, H.J. Kim, E.B. Bae, W.T. Cho, Y. Choi, S.H. Hwang, C.M. Jeong, J.B. Huh, Evaluation of 1-ethyl-3-(3-dimethylaminopropyl) carbodiimide cross-linked collagen membranes for guided bone regeneration in beagle dogs, Materials 13 (2020) 4599, https://doi.org/10.3390/ma13204599.
[49] X. Zhao, X. Li, X. Xie, J. Lei, L. Ge, L. Yuan, D. Li, C. Mu, Controlling the pore structure of collagen sponge by adjusting the cross-linking degree for construction of heterogeneous double-layer bone barrier membranes, ACS Appl. Bio Mater. 3 (2020) 2058–2067, https://doi.org/10.1021/acsabm.9b01175.
[50] A. Sorushanova, L.M. Delgado, Z. Wu, N. Shologu, A. Kshirsagar, R. Raghunath, A. M. Mullen, Y. Bayon, A. Pandit, M. Raghunath, D.I. Zeugolis, The collagen suprafamily: from biosynthesis to advanced biomaterial development, Adv. Mater. 31 (2019), e1801651, https://doi.org/10.1002/adma.201801651.
[51] B. Lynch, S. Bancelin, C. Bonod-Bidaud, J.B. Gueusquin, F. Ruggiero, M. C. Schanne-Klein, J.M. Allain, A novel microstructural interpretation for the biomechanics of mouse skin derived from multiscale characterization, Acta Biomater. 50 (2017) 302–311, https://doi.org/10.1016/j.actbio.2016.12.051.
[52] I. Jorba, G. Beltran, B. Falcones, B. Suki, R. Farre, J.M. Garcia-Aznar, D. Navajas, Nonlinear elasticity of the lung extracellular microenvironment is regulated by macroscale tissue strain, Acta Biomater. 92 (2019) 265–276, https://doi.org/10.1016/j.actbio.2019.05.023.
[53] M.D.A. Norman, S.A. Ferreira, G.M. Jowett, L. Bozec, E. Gentleman, Measuring the elastic modulus of soft culture surfaces and three-dimensional hydrogels using atomic force microscopy, Nat. Protoc. 16 (2021) 2418–2449, https://doi.org/10.1038/s41596-021-00495-4.
[54] L. Qian, H. Zhao, Nanoindentation of soft biological materials, Micromachines 9 (2018), https://doi.org/10.3390/mi9120654.

[55] P.N. Nonaka, N. Campillo, J.J. Uriarte, E. Garreta, E. Melo, L.V. de Oliveira, D. Navajas, R. Farre, Effects of freezing/thawing on the mechanical properties of decellularized lungs, J. Biomed. Mater. Res. A. 102 (2014) 413–419, https://doi.org/10.1002/jbm.a.34708.
[56] B. Gurumurthy, A.V. Janorkar, Improvements in mechanical properties of collagen-based scaffolds for tissue engineering, Curr. Opin. Biomed. Eng. 17 (2021), 100253, https://doi.org/10.1016/j.cobme.2020.100253.
[57] R. Tonndorf, D. Aibibu, C. Cherif, Collagen multifilament spinning, Mater. Sci. Eng. C. Mater. Biol. Appl. 106 (2020), 110105, https://doi.org/10.1016/j.msec.2019.110105.
[58] A. Gautieri, S. Vesentini, A. Redaelli, M.J. Buehler, Hierarchical structure and nanomechanics of collagen microfibrils from the atomistic scale up, Nano Lett. 11 (2011) 757–766, https://doi.org/10.1021/nl103943u.
[59] K.L. Lee, M. Sobieraj, M. Baldassarri, N. Gupta, D. Pinisetty, M.N. Janal, N. Tovar, P.G. Coelho, The effects of loading conditions and specimen environment on the nanomechanical response of canine cortical bone, Mater. Sci. Eng. C. Mater. Biol. Appl. 33 (2013) 4582–4586, https://doi.org/10.1016/j.msec.2013.07.018.
[60] S.P. Roth, S.M. Glauche, A. Plenge, I. Erbe, S. Heller, J. Burk, Automated freeze-thaw cycles for decellularization of tendon tissue - a pilot study, BMC Biotechnol. 17 (2017) 13, https://doi.org/10.1186/s12896-017-0329-6.
[61] A. Mazurkiewicz, The effect of trabecular bone storage method on its elastic properties, Acta Bioeng. Biomech. 20 (2018) 21–27, https://doi.org/10.5277/Abb-00967-2017-03.
[62] S. Camarero-Espinosa, M. Carlos-Oliveira, H. Liu, J.F. Mano, N. Bouvy, L. Moroni, 3D printed dual-porosity scaffolds: the combined effect of stiffness and porosity in the modulation of macrophage polarization, Adv. Healthc. Mater. 11 (2022), e2101415, https://doi.org/10.1002/adhm.202101415.
[63] P.A. Janmey, D.A. Fletcher, C.A. Reinhart-King, Stiffness sensing by cells, Physiol. Rev. 100 (2020) 695–724, https://doi.org/10.1152/physrev.00013.2019.
[64] Y. Zhu, H. Liang, X. Liu, J. Wu, C. Yang, T.M. Wong, K.Y.H. Kwan, K.M.C. Cheung, S. Wu, K.W.K. Yeung, Regulation of macrophage polarization through surface topography design to facilitate implant-to-bone osteointegration, Sci. Adv. 7 (2021), https://doi.org/10.1126/sciadv.abf6654 eabf6654.
[65] C.P. Chang, Y.C. Su, P.H. Lee, H.Y. Lei, Targeting NFKB by autophagy to polarize hepatoma-associated macrophage differentiation, Autophagy 9 (2013) 619–621, https://doi.org/10.4161/auto.23546.
[66] K.H. Vining, A.E. Marneth, K. Adu-Berchie, J.M. Grolman, C.M. Tringides, Y. Liu, W.J. Wong, O. Pozdnyakova, M. Severgnini, A. Stafford, G.N. Duda, F.S. Hodi, A. Mullally, K.W. Wucherpfennig, D.J. Mooney, Mechanical checkpoint regulates monocyte differentiation in fibrotic niches, Nat. Mater. 21 (2022) 939–950, https://doi.org/10.1038/s41563-022-01293-3.
[67] T. Lecuit, A.S. Yap, E-cadherin junctions as active mechanical integrators in tissue dynamics, Nat. Cell Biol. 17 (2015) 533–539, https://doi.org/10.1038/ncb3136.
[68] J.Z. Kechagia, J. Ivaska, P. Roca-Cusachs, Integrins as biomechanical sensors of the microenvironment, Nat. Rev. Mol. Cell Biol. 20 (2019) 457–473, https://doi.org/10.1038/s41580-019-0134-2.
[69] M.K.L. Han, J. de Rooij, Converging and unique mechanisms of mechanotransduction at adhesion sites, Trends Cell Biol. 26 (2016) 612–623, https://doi.org/10.1016/j.tcb.2016.03.005.
[70] B. Guo, X. Feng, Y. Wang, X. Wang, Y. He, Biomimetic and immunomodulatory baicalin-loaded graphene oxide-demineralized bone matrix scaffold for in vivo bone regeneration, J. Mater. Chem. B 9 (2021) 9720–9733, https://doi.org/10.1039/d1tb00618e.
[71] D. Zhang, Q. Chen, C. Shi, M. Chen, K. Ma, J. Wan, R. Liu, Dealing with the foreign-body response to implanted biomaterials: strategies and applications of new materials, Adv. Funct. Mater. 31 (2021), 2007226.
[72] L. Crawford, M. Wyatt, J. Bryers, B. Ratner, Biocompatibility evolves: phenomenology to toxicology to regeneration, Adv. Healthc. Mater. 10 (2021), e2002153, https://doi.org/10.1002/adhm.202002153.
[73] O. Veiseh, A.J. Vegas, Domesticating the foreign body response: recent advances and applications, Adv. Drug Deliv. Rev. 144 (2019) 148–161, https://doi.org/10.1016/j.addr.2019.08.010.
[74] J. Fang, R. Liu, S. Chen, Q. Liu, H. Cai, Y. Lin, Z. Chen, Z. Chen, Tuning the immune reaction to manipulate the cell-mediated degradation of a collagen barrier membrane, Acta Biomater. 109 (2020) 95–108, https://doi.org/10.1016/j.actbio.2020.03.038.
[75] E. Calciolari, F. Ravanetti, A. Strange, N. Mardas, L. Bozec, A. Cacchioli, N. Kostomitsopoulos, N. Donos, Degradation pattern of a porcine collagen membrane in an in vivo model of guided bone regeneration, J. Periodontal. Res. 53 (2018) 430–439, https://doi.org/10.1111/jre.12530.
[76] S. Ullah, X. Chen, Fabrication, applications and challenges of natural biomaterials in tissue engineering, Appl. Mater. Today 20 (2020), 100656, https://doi.org/10.1016/j.apmt.2020.100656.
[77] Z.J. Feng, Q. Su, C.N. Zhang, P.S. Huang, H.J. Song, A.J. Dong, D.L. Kong, W. W. Wang, Bioinspired nanofibrous glycopeptide hydrogel dressing for accelerating wound healing: a cytokine-free, M2-type macrophage polarization approach, Adv. Funct. Mater. 30 (2020) 13, https://doi.org/10.1002/adfm.202006454.
[78] G.Y. Guo, T. Gong, H. Shen, Q.J. Wang, F. Jiang, J. Tang, X.W. Jiang, J.X. Wang, X. L. Zhang, W.B. Bu, Self-amplification immunomodulatory strategy for tissue regeneration in diabetes based on cytokine-ZIFs system, Adv. Funct. Mater. 31 (2021), 2100795, https://doi.org/10.1002/adfm.202100795.
[79] W. Qiao, H. Xie, J. Fang, J. Shen, W. Li, D. Shen, J. Wu, S. Wu, X. Liu, Y. Zheng, K. M.C. Cheung, K.W.K. Yeung, Sequential activation of heterogeneous macrophage phenotypes is essential for biomaterials-induced bone regeneration, Biomaterials 276 (2021), 121038, https://doi.org/10.1016/j.biomaterials.2021.121038.
[80] M. Rahmati, J.J. Blaker, S.P. Lyngstadaas, J.F. Mano, H.J. Haugen, Designing multigradient biomaterials for skin regeneration, Mater, Today. Adv. 5 (2020), 100051, https://doi.org/10.1016/j.mtadv.2019.100051.
[81] M.L. Crichton, X. Chen, H. Huang, M.A.F. Kendall, Elastic modulus and viscoelastic properties of full thickness skin characterised at micro scales, Biomaterials 34 (2013) 2087–2097, https://doi.org/10.1016/j.biomaterials.2012.11.035.
[82] E. Guan, S. Smilow, M. Rafailovich, J. Sokolov, Determining the mechanical properties of rat skin with digital image speckle correlation, Dermatology 208 (2004) 112–119, https://doi.org/10.1159/000076483.
[83] İ. Özyazgan, N. Liman, N. Dursun, I. Güneş, The effects of ovariectomy on the mechanical properties of skin in rats, Maturitas 43 (2002) 65–74, https://doi.org/10.1016/S0378-5122(02)00181-0.
[84] K.K. Zheng, Y. Tong, S.H. Zhang, R.Y. He, L. Xiao, Z. Iqbal, Y.H. Zhang, J. Gao, L. Zhang, L.B. Jiang, Y.L. Li, Flexible bicolorimetric polyacrylamide/chitosan hydrogels for smart real-time monitoring and promotion of wound healing, Adv. Funct. Mater. 31 (2021), 2102599, https://doi.org/10.1002/adfm.202102599.